TWO-PHASE FLOW AND HEAT TRANSFER IN PIN-FIN ENHANCED MICRO-GAPS

A Thesis
Presented to
The Academic Faculty

by

Steven A. Isaacs

In Partial Fulfillment
of the Requirements for the Degree
Master of Science in the
School of Mechanical Engineering

Georgia Institute of Technology
December 2013

TWO-PHASE FLOW AND HEAT TRANSFER IN PIN-FIN ENHANCED MICRO-GAPS

Approved by:

Dr. Yogendra Joshi, Advisor
School of Mechanical Engineering
Georgia Institute of Technology

Dr. Muhannad Bakir
School of Electrical and Computer Engineering
Georgia Institute of Technology

Dr. Andrei Fedorov
School of Mechanical Engineering
Georgia Institute of Technology

Date Approved: August 5th, 2013

ACKNOWLEDGEMENTS

I would like to thank my advisor, Dr. Yogendra Joshi for his guidance and support throughout the graduate process and whose continuous encouragement and mentoring has allowed me to reach my current position in my career. I would also like to thank my committee members, Dr. Muhannad Bakir and Dr. Andrei Fedorov for serving on my committee and their support throughout my research efforts.

I want to thank all of my fellow colleagues in the Microelectronics & Emerging Technologies Thermal Laboratory (METTL) and Consortium for Energy Efficient Thermal Management (CEETHERM) Laboratory. I have been blessed to a part of this lab group and the friendships and intellectual conversations they have provided have been unparalleled. In particular, I want to thank Dr. Yoon Jo Kim for his guidance in construction of the testing platform. I would also like to thank Dr. Muhannad Bakir and Ms. Yue Zhang for fabricating all of the test samples and willingness to work closely with me when I needed assistance. I would also like to thank Dr. Minami Yoda for generously providing access to the high speed camera used throughout this study.

Above all, I would like to thank my family for their support. In particular, I want to thank my mother, Dr. Nelda Isaacs whose passion for academia and unconditional love is the only reason I have made it this far. Lastly, I want to thank my late father, Mr. Mac Isaacs who instilled in me my passion for curiosity and engineering. This work is dedicated to him.

TABLE OF CONTENTS

LIST OF TABLES

LIST OF FIGURES

NOMENCLATURE

A_b	array base area (m^2)
$A_{c,fin}$	cross sectional area of fin (m^2)
$A_{e,b}$	array base area exposed to fluid (m^2)
$A_{e,fin}$	fin area exposed to fluid (m^2)
c	temperature coefficient ($/^oC$)
c_p	specific heat (kJ/kgK)
D	diameter of fin (m)
dP	differential pressure (Pa)
dx	differential distance (m)
G	cross sectional area of fin (kg/m^2s)
h	heat transfer coefficient (W/m^2K)
$h_{f_{out}}$	enthalpy of saturated liquid at outlet (kJ/kg)
$h_{g_{out}}$	enthalpy of saturated vapor at outlet (kJ/kg)
h_{in}	enthalpy of fluid at inlet (kJ/kg)
h_{out}	enthalpy of fluid at outlet (kJ/kg)
I	current (A)
k	fin thermal conductivity (W/mK)
L_b	array base length (m)
L_f	fin length (m)
$L_{f,corr}$	corrected fin length (m)
N	number of fins
P	fin perimeter (m)
q_{eff}	effective heat load (W)

q_{total}	total power into heater (W)
$\dot{m}$	mass flowrate (kg/s)
q	heat load (W)
R	electrical resistance (Ω)
R_o	reference electrical resistance (Ω)
Re	Reynolds number
T_{in}	inlet temperature of fluid (K)
T_{out}	outlet temperature of fluid (K)
T_w	array base temperature (K)
T_∞	saturation or average fluid temperature (K)
ΔT	change in temperature (K)
u	superficial velocity (m/s)
x	vapor quality

Symbols

α	tube angle from horizontal (^{o})
η	fin efficiency
ρ	density (kg/m^3)

Subscripts

G	vapor phase
L	liquid phase
S	single phase

SUMMARY

Two-phase cooling methods could become the next techniques for high heat removal from high power density electronic packages such as three-dimensionally stacked chips. The small size and unique geometry of such applications makes the existing heat transfer and pressure drop correlations inapplicable. These configurations must be tested experimentally to determine their hydraulic and thermal performance. The focus of the present study is to experimentally determine two-phase performance of surface enhanced micro-gaps.

The beginning of this thesis deals with the introduction of microfluidic cooling methods. In particular microchannel and enhanced micro-gap geometries are considered. Also, comparison between water and dielectric working fluids is made. A brief overview of flow boiling regime definition is provided, along with relevant flow regime mapping techniques.

Next, the pin fin sample and flow loop testing platform utilized in the present work are discussed. A brief description of the fabrication of the single and multi-heater samples is provided. Unique features of the fabrication and assembly process are described. A detailed description of the setup and operation of the flow loop are discussed. The general experimental procedure provides information on key steps performed for every experiment.

The final section reports the experimental results. A parametric study for each sample is performed by varying heat flux and flowrate. Thermal performance and flow visualization results for both uniformly and partially heat samples are presented and

analyzed. Key trends in heat transfer coefficient data and physical features of the two-phase flow are highlighted. Flow regimes and boiling mechanisms are determined.

CHAPTER 1

INTRODUCTION

Modern electronic devices are rapidly becoming more compact and multi-functional. Particularly, with the advent of 3D, stacked architectures, power densities of these devices are continually increasing, much in accordance with Moore's Law. The need for high heat dissipation cooling methods is crucial and much effort has been exerted in developing these. Microchannel and pin fin enhanced surfaces are commonly utilized in many macroscale heat exchangers. Thanks to the development of micro fabrication techniques, these enhanced features can be easily implemented at the microscale, and are promising options for heat removal from high power density electronic packaging.

Two different categories of working fluids are commonly used for flow boiling based cooling methods, each with its own advantages and disadvantages; water and dielectric fluids [1]. Water has favorable liquid thermal properties, extensive characterization literature and is readily available. Despite its superior heat transfer performance, water has potential disadvantages when used for electronic cooling, if dielectric strength cannot be maintained these include corrosion and possible shorting in the case of leakage. Dielectric fluids, on the other hand, are electrically inert and and can be selected to achieve saturation temperatures closer to maximum allowable chip temperatures, which is not possible with water. Various dielectric fluids such as refrigerants and other novel fluid mixtures continue to be a current research thrust in microelectronic cooling. The following review reveals relevant studies on microchannel

and micro-gap geometries utilizing various working fluids. Also, a brief introduction to two-phase flow regimes maps is provided.

1.1 Mircochannels

Microchannels have been extensively studied within the last 3 decades with focus on determination of heat transfer coefficient, *h*, as well as critical heat flux (CHF), flow patterns and modeling. Both water and dielectric fluids have been investigated. Water has the advantage of a relatively high thermal conductivity; however, it can be detrimental to an electronic system if leaks develop. Dielectric fluids are non-conductive and are often a more realistic, direct-contact method for cooling from an application standpoint.

In 1981, the pioneering study of single-phase cooling with microchannels was conducted by Tuckerman and Pease [2]. This work demonstrated the low thermal resistance that can be achieved with liquid cooling through microchannels using water. However, single-phase flows are associated with large temperature gradients along the channel length and, accordingly, larger flowrates. Table 1.1 shows a comparison of single and two-phase flow studies in microchannels. A major consequence under single-phase conditions is a larger associated flowrate relative to two-phase conditions for identical heat removal. In single-phase conditions heat is transfered via sensible heat resulting in a large temperature rise along the microchannel. Two-phase conditions rely on heat transfer via latent heat, in which fluid temperature remains nearly uniform during the boiling process. Therefore, for an identical heat flux a microchannel operating under two-phase conditions requires a lower flowrate and results in a lower surface temperature relative to a microchannel operating under single-phase conditions.

Table 1.1.1 Selected single and two-phase microchannel studies

	Material	**Dimensions (A_c/L in mm)**	**Liquid**	**Q (l/min)**	**$\Delta P/\Delta L$ (kPa/m)**	**Phase**
Tuckerman et al.[2]	Si	0.0018	Water	0.282	11000	Single
Tuckerman et al.[2]	Si	0.0015	Water	0.516	22000	Single
Pijnenburg et al.[3]	Si	0.0020	Water	1.1	17200	Single
Qu & Mudawar[4]	Cu	0.0037	Water	0.058	34	Two
Qu & Mudawar[5]	Cu	0.0039	Water	0.051	39.1	Two

Bowers and Mudawar investigated two-phase flow through minichannel and microchannel heat sinks, reporting a critical heat flux (CHF) above 200 W/cm^2 [6]. A comprehensive review of flow boiling in microchannels can also be found in literature [5], [7], [8]. Numerous studies involving the modeling of heat transfer and bubble growth have also been performed. For example, Thome et al developed a model to predict local *h* during slug flow [9], [10]. Mukherjee et al developed a numerical model to predict bubble growth [11]. A major drawback to two-phase cooling in microchannel heat sinks is flow instability. Qu and Mudawar reported flow instabilities due to pressure drop oscillations that resulted in pre-mature CHF [5]. Numerous papers have been published concerning the suppression and stabilization of this phenomena [12], [13], [14], [15] . A comprehensive evaluation of microchannel cooling methods can be found in literature [16].

Since flow through microchannel arrays comes with inherent complexities like high temperature gradients and flow instabilities, micro-gaps utilizing augmentation features such as micro pin fins have surfaced as a promising alternative.

1.2 Pin Fin Arrays

To date, a limited amount of literature on the topic of heat transfer and flow over micro pin fin arrays within micro-gaps exists. However, this is a quickly growing area of research. Evaluation of micro pin fin arrays shows a potential advantage over microchannel configurations [17], [18], [19]. According to Peles et al, at a similar pressure drop and heat flux, a micro pin fin heat sink provides a minimum total thermal resistance of 0.0389 K/W while a microchannel heat sink provides a minimum of 0.0900 K/W [17]. Experimental values of h near 55 kW/m^{2}K were recorded for single-phase deionized water [18]. Nusselt number correlations for large scale pin fin geometries were compared and observed to over-predict the experiemental data by a factor as high as 2 for low Reynolds number flows (~100). Endwall effects between the pin fins and adjacent walls of the channel imposed boundary layers within the array. With a microscale channel and fin heights, these boundary layers were attributed to the reduced Nusselt numbers at low Reynolds numbers. Suppression of flow separation was also identified as negatively impacting h in smaller devices.

Qu demonstrated decreased thermal resistances using pin fin arrays with strong dependence on liquid flowrate but highlighted the coupled higher pressure drops compared to microchannels [19]. Another comprehensive experimental study identified a lower thermal resistance for a given flowrate using staggered pin fin enhancements compared with other geometries such as inline pin fin, parallel plates, and microchannels [20]. Using a device that was based on vertically integrated chip stacks and that contained electrical interconnect-compatible pin fins, heat fluxes >200 W/cm^2 were dissipated at a maximum junction temperature of 80^{o}C considering double-sided heating. This study

also demonstrated multi-tier cooling capabilities for use in 3D chip stacks. This study emphasized that hydraulic performance should also be stressed when evaluating effective types of pin fin geometries. Specifically, a tradeoff exists between thermal and hydraulic performances [21]. Though pin fin geometries that promote flow separation and mixing result in lower thermal resistances, a high pressure drop is encountered, negatively impacting pumping power. Accordingly, the staggered pin fin orientation has moderate thermal and hydraulic performance and may be a more realistic geometry in terms of application.

One of the earliest studies on using a dielectric fluid flow over micro pin fin arrays looked at single-phase and flow boiling inception [22]. Using a 1,800μm x 10,000μm array of 100μm diameter staggered fins and gap height of 243μm, indicated Nusselt Number values greater than 20 using refrigerant R-123 as a working fluid. Qu et al demonstrated h as high as 180 kW/m^{2}K with 200μm x 200μm staggered square pins with a height of 670μm [23]. Krishnamurthy et al reported a local h as high as 75 kW/m^{2}K using a bank of staggered, circular pin fins with a diameter of 100μm and height of 250μm. It should also be noted that, instead of considering these flow passage enhancements separately, studies have also delved into a combination of microchannel and micro pin fin enhancement [24]. One primary application of pin fin structures is in 3D chips stacks in which pin fins also serve as through silicon vias (TSV) for electrical connections between individual tiers [25].

1.3 Flow Boiling Regimes

In conjunction with thermal and hydrodynamic studies, flow morphology is a key factor in completely defining the particular heat transfer mechanisms that occur for given

flow conditions. Flow morphology is used along with heat transfer data to elucidate a clear description of how heat is transferred between the array and fluid. For macroscale sizes, there are generally six separate flow patterns identified with flow boiling through a horizontally oriented heated tube and are shown in Figure 1.3.1 [26]. These flow patterns are also used to describe two-phase flow through channels of various geometry including pin-fin arrays.

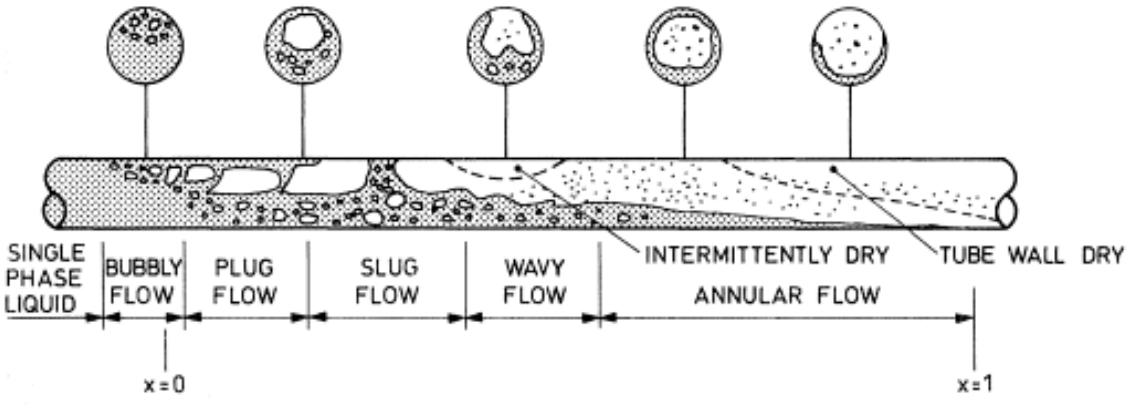

Figure 1.3.1 Two-phase flow regimes in horizontal tube [26]

At low vapor quality, small, discrete bubbles develop at bubble departure sites, detach from the heated surface and are entrained within the liquid phase. These vapor bubbles are small relative to the size of the tube. This is termed *bubbly flow*. As vapor quality increases, these bubbles begin to coalesce and these larger vapor bubbles are closer in size relative to the channel and tend to travel along the top of the tube. While these vapor bubbles travel through the tube they are separated by liquid slugs. A liquid film separates the vapor bubbles from the tube wall. This is termed *plug flow*. A flow regime termed *stratified flow* is observed for low liquid and vapor velocities in which liquid resides along the bottom of the tube and vapor along the top. The liquid-vapor interface is smooth. As vapor quality increases, the liquid-vapor interface transitions from a flat,

smooth shape to a wavy shape due to an increase in vapor velocity. This is termed *wavy flow*. As vapor velocity further increases, the wave-shaped interface increases in amplitude to a point where the liquid peaks are in contact with the upper surface of the tube. This results in a sequence of vapor slugs flowing through the tube. This is termed *slug flow*. For even higher vapor velocities, the flow transitions to one that contains a continuous vapor core surrounded by a liquid film. This liquid film is in contact with the tube's inner surface. Due to gravitational forces, the liquid film towards the bottom of the tube is thicker than towards the top. However, for very high vapor velocities initial forces are much greater than gravitational forces and the annular liquid film thickness is closer to uniformity. This is termed *annular flow*. As vapor quality further increases, the liquid film thickness decreases due to evaporation. On some areas of the heated surface the liquid film ceases to exist and the vapor core comes in contact with the surface. This occurs periodically and is term *intermittent dry-out*. After complete evaporation of the liquid film the entire heated surface comes in contact with the vapor phase.

The next step after flow regime definition is the development of methods to define transition regions between different regimes based on experimental parameters. This is known regime mapping. Transition regions are defined empirically as well as analytically.

1.4 Regime Mapping

Regime mapping has been established and well documented in flow boiling through pipes and microchannels. Many current research efforts continue to develop and establish regime mapping concerning flow boiling over pin-fin arrays. Typically, regime maps are constructed with nondimensional parameters or superficial velocities as the X

and Y coordinates. Transitions between flow boiling regimes are determined analytically and empirically. Regime map values calculated from this study were compared with both analytically and experimentally defined transitions. This allowed comparison to relevant experiments in literature and predictive methods of flow regime determination.

Several analytical methods to predict the various transitions between the identified flow regimes have been proposed in literature. The method proposed by Taitel and Dukler is one of the more promising methods [27]. This innovative approach to flow regime mapping utilizes common nondimensional parameters and physics-based transition criteria and does not rely on empirical formulations (Figure 1.4.1).

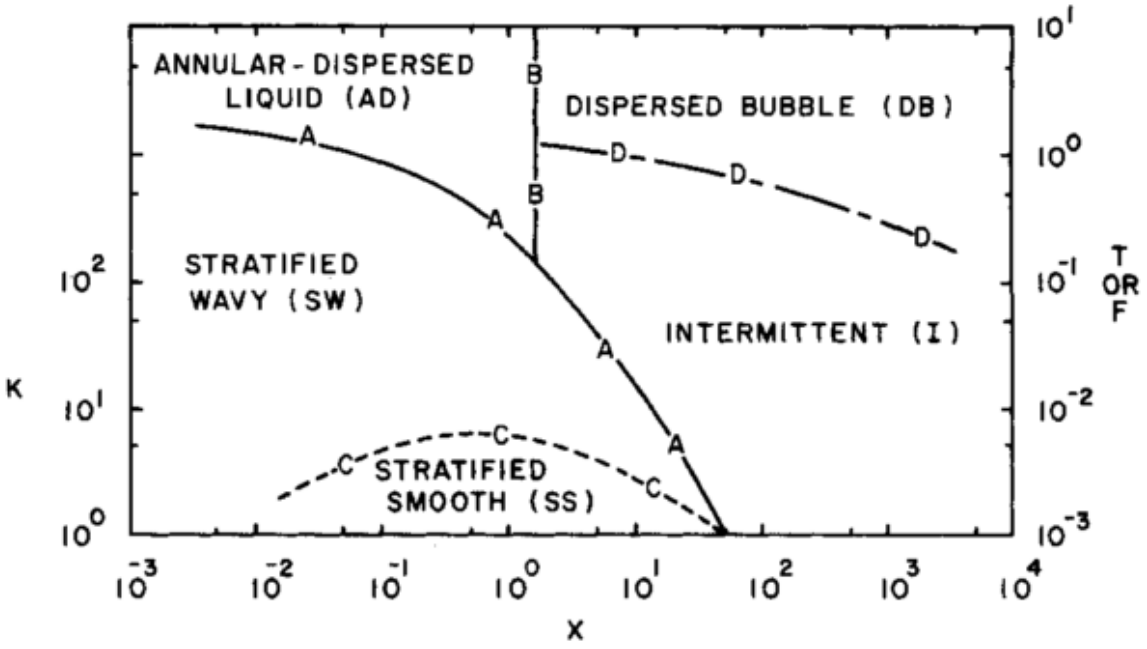

Figure 1.4.1 Flow regime map for horizontal two-phase flow [27].

Since the Taitel-Dukler maps were developed for macro sizes, it is important to compare results from this study on micro-gaps to this predictive method. Only a brief description of the theoretical method will be described next, enough to facilitate comparison to the

experimental results of this study. A detailed description and formulation of the method can be found in the reference.

From a dimensionless transformation of the momentum balance of each phase in the tube, two dimensionless parameters are formed; the Martinelli parameter, *X*, and *Y*.

$$X^2 = \frac{|dP/dx_{L^s}|}{|dP/dx_{G^s}|} \tag{1.1}$$

$$Y = \frac{(\rho_L - \rho_G)\, g \sin\alpha}{|dP/dx_{G^s}|} \tag{1.2}$$

Y is equal to zero for flow through horizontal tubes. The Martinelli parameter is the ratio of pressure drop of each phase in the tube and can be calculated with knowledge of flowrate, diameter, and fluid properties. This parameter is used as the horizontal axis of the flow regime map. The modified Froude number

$$F = \sqrt{\frac{\rho_G}{(\rho_L - \rho_G)}} \frac{{u_G}^s}{\sqrt{D\, g\, cos\alpha}} \tag{1.3}$$

is used with transition criterion based on Kelvin-Helmholtz stability criterion to model the transition between stratified and intermittent or annular-dispersed liquid regimes. This transition is shown by line "A" in Figure 1.4.1. Criterion based on liquid level in the tube is used to form line "B" at X = 1.6. This predicts transition between intermittent and annular dispersed liquid regimes. The dimensionless parameter *K* is defined as

$$K^2 = F^2 Re_{L^s} \tag{1.4}$$

and is used with criterion based on wave generation to define the boundary between stratified smooth and stratified wavy regimes (line "C"). The parameter *T* is defined as

$$T^2 = \left[\frac{|dP/dx_{L^s}|}{(\rho_L - \rho_G)\, g \cos\alpha}\right] \tag{1.5}$$

Using criterion based on the balance between buoyant forces and forces resulting from turbulent fluctuations, the boundary identifying the transition between intermittent and dispersed bubble regimes is shown as line “D”.

The experimental form of regime mapping is accomplished through flow boiling regime mapping in which the goal is to distinguish, visually, how the vapor and liquid regions are oriented along the channel or array. Common experimental techniques involve the calculation of superficial liquid and vapor velocities for given conditions and subsequent comparison with flow imaging. Plots are developed in which various flow patterns are illustrated based on flow visualization. Transition regions on plots indicate transition from one type of morphology to another. Many studies have been performed in order to build a database that considers a wide variety of channel and fin geometries, heat fluxes, flowrates, pressure drops, and working fluids.

This study aims to broaden the experimental knowledge base of two-phase flow over micro pin fin arrays. Current literature only supports micro pin fin arrays placed in relatively narrow channels (~2mm x 1cm width) while there is no literature supporting studies on micro pin fin enhanced micro-gaps placed on larger, chip-sized areas (1cm x 1cm). Also, the particular working fluid used in this study, R245fa, has yet to be studied for this type of scale and surface enhancement geometry. Furthermore, this study considers experimental investigation on partial heating of two-phase, pin fin enhanced micro-gaps which have little representation in literature. Results are analyzed and compared with other studies and predictive methods.

CHAPTER 2

DEVICE AND EXPERIMENTAL OVERVIEW

The experimental platform used in this study consisted of a cleanroom fabricated, silicon, diabatic, pin fin sample and a closed, flow loop. The samples were designed and fabricated by the Bakir group at Georgia Tech. The process involved etching and film deposition to produce the pin fin array, platinum heaters and copper lines [25]. The samples were tested in a closed flow loop, where temperature and pressure measurements allowed for thermal and hydrodynamic performance evaluation.

2.1 Pin Fin Device

The micro pin arrays were populated on a 1cm x 1cm square surface that included inlet and outlet flow passages. The height, pitch and diameter of the pins were 200μm, 225μm, and 150μm, respectively (Figure 2.1.1). The pins were located in 43 rows with 42 pins per row. Based on thermal and hydrodynamic studies from literature, this study implemented a staggered pin fin orientation. In order to simulate uniform and partial microprocessor heating, platinum heaters, in a spiral pattern, were fabricated into the sample directly behind the pin fin surface. Once samples were fabricated in the cleanroom, the next steps involved attachment of the glass cover and nanoports, calibration of the heaters, and soldered leads.

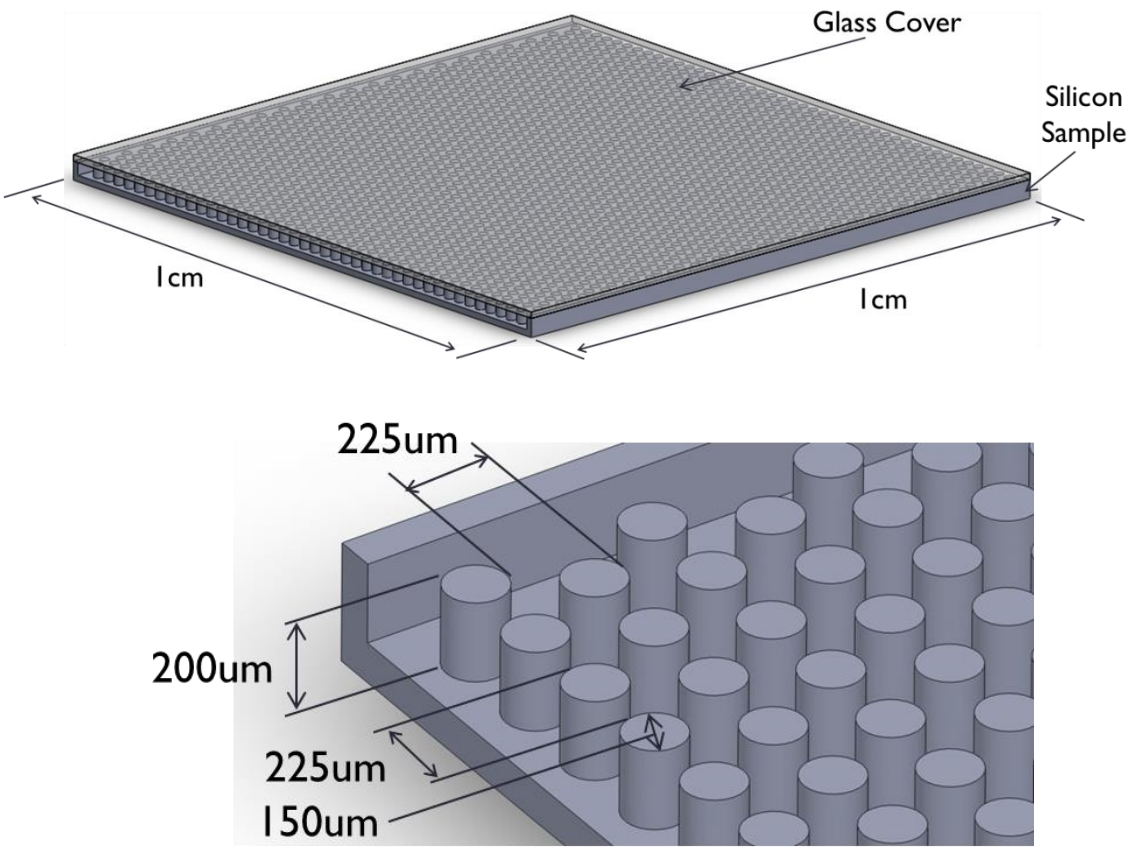

Figure 2.1.1 Staggered pin fin array diagram

A clear, glass cover was bonded to the top of the pins. This had two main purposes. The first was to completely seal the pins and flow passages. The second was to provide a means of visualizing flow through the sample during experiments. Two different types of heater patterns were tested, single and multi-heater. Single heater samples (Figure 2.1.5) consisted of one heater that was deposited over the entire array base. This allowed for uniform heating simulation as well as average wall temperature measurements. The multi-heater patterns consisted of four heaters covering each quadrant of the array base (Figure 2.1.6). This allowed for the capability of partial heating and local wall temperature measurements.

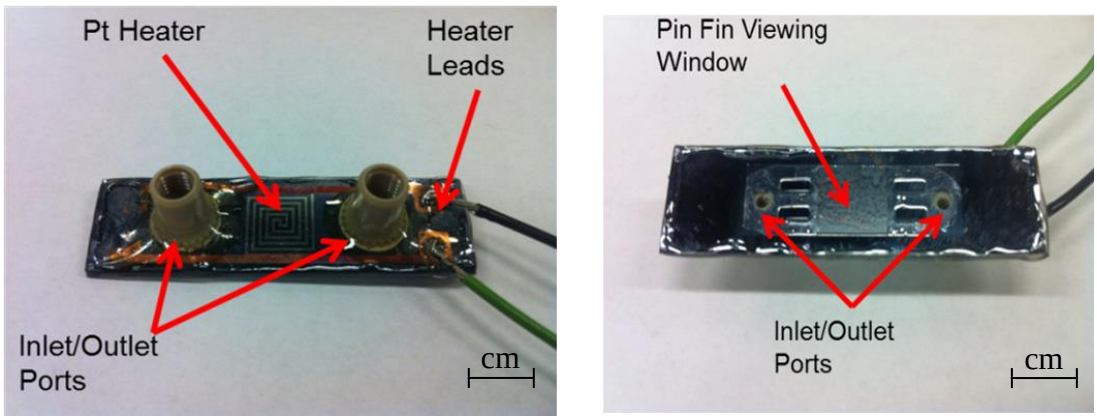

Figure 2.1.2 Single heater pin fin sample

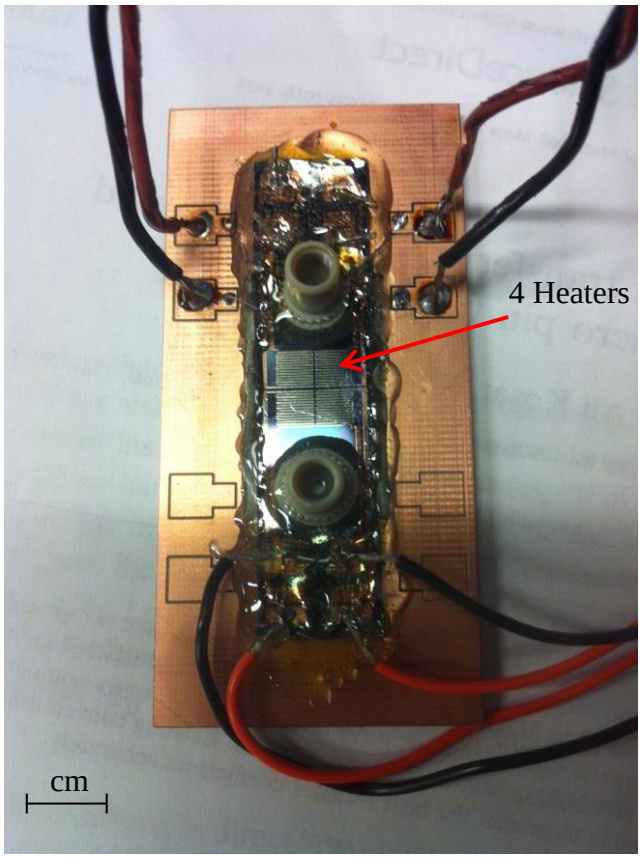

Figure 2.1.3 Multi-heater pin fin sample with printed circuit board

Each heater, regardless of pattern, had 1.5μm thick copper lines running to larger copper pads located near the edges of the sample where soldered leads were attached. These leads then attached to a power supply. A printed circuit board (PCB) board was designed

with large (5mmx10mm) pads and a viewing window. The pin fin sample was mounted on the PCB with the pin fin array aligning with the viewing window and copper pads adjacent to the large PBC pads (Figure 2.1.6). The power supply wires were soldered to the PCB pads and smaller copper wires were soldered from the PCB pads to the samples pads. This provided more stability and control during the soldering process.

Sample Reliability

Due to the novel pin fin samples used in this study, the reliability played a vital role in the fabrication, assembly and experimental testing. A few different reliability factors including flow bypass, powering of the heaters and flow leakage were encountered.

The initial attachment of the clear, glass cover to the silicon sample proved to be a challenge in that the control, from sample to sample, did not consistently seal the array correctly. The process involved applying an epoxy layer to the sample side and attaching the glass cover and allowing the assembly to cure for 24 hours. Early samples showed inconsistencies in the final position of the epoxy layer. This often resulted in flow bypassing the pin fin array, meandering its way up the side walls and flowing through gaps in the epoxy layer in between the silicon and glass cover. Since this bypass of fluid resulted in incorrect flowrate measurements over the array, an additional step was added to the bonding process. Figure 2.1.2 displays one example of this sealing issue.

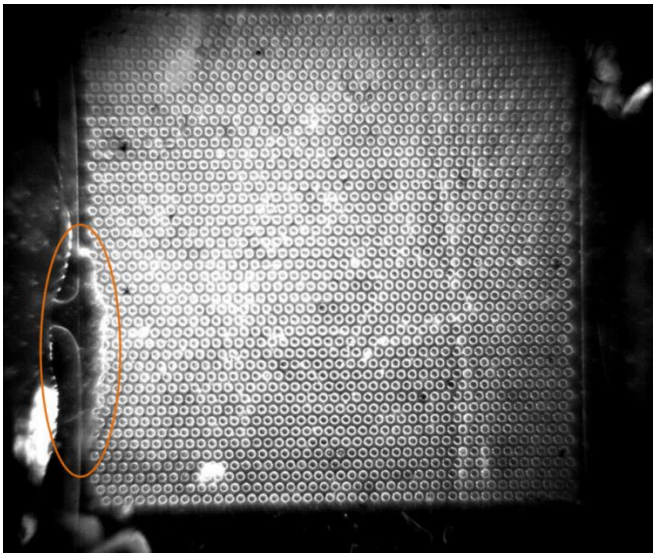

Figure 2.1.4 Image of flow bypass

In order to address this defect, an additional clamping process was included during the sample fabrication. First, epoxy was placed only at the region between the pin fin array and sample edge. This region was then clamped and allowed to cure. Once cured, the remaining edges of the sample were bonded, until the entire sample was sealed. Figure 2.1.3 shows a schematic comparing a sample containing flow bypass and a sample after the clamping process was implemented. Figure 2.1.4 displays images of the clamping process.

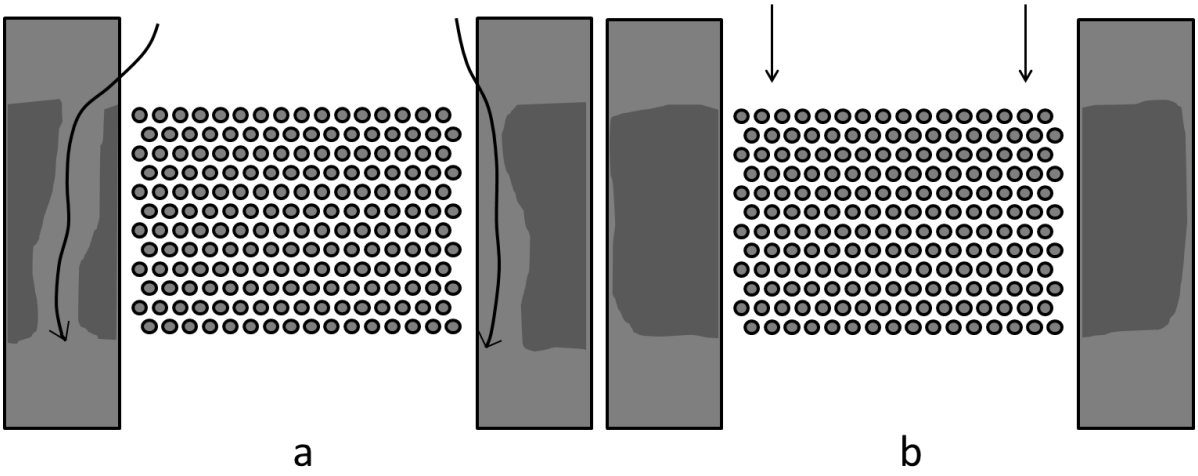

Figure 2.1.5 Diagram of sample a) with flow bypass and b) after clamping process

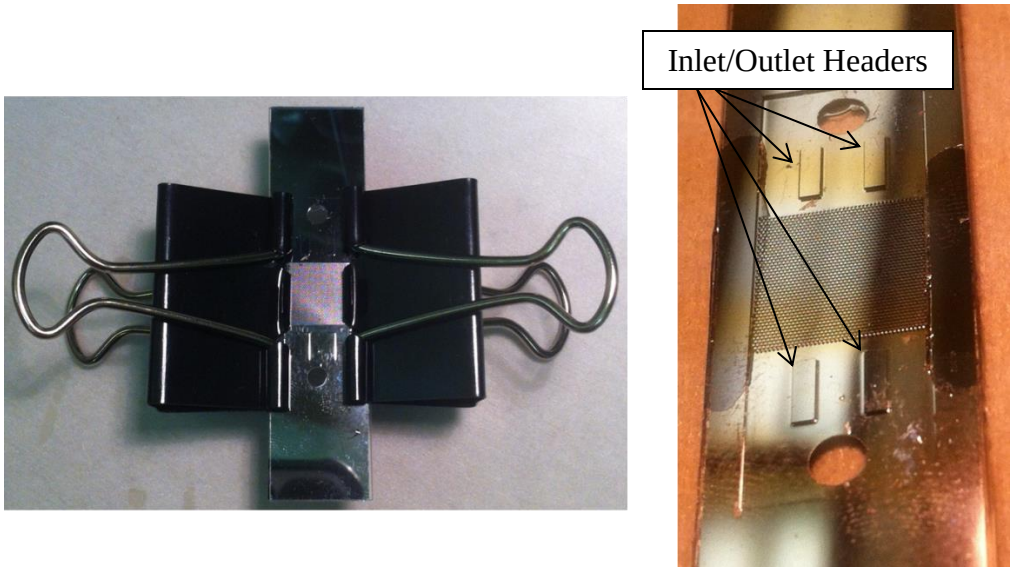

Figure 2.1.6 Clamping process

Once this step was completed, epoxy was placed along the edges of the sample and nanoports so that the entire sample was sealed.

Though Figure 2.1.5 shows successful soldering of power supply wire directly to the sample's copper pads, this process was not easily repeatable. On occasion, the copper pad would delaminate during the soldering process. This was believed to be due to the

large mass of the power supply wire (10 awg) relative to the very thin copper pad. Accordingly, an extra step in the assembly process was included to deter the delamination of the copper pads. This step involved the implementation of a PCB that was bonded to the pin fin sample. The PCB contained much thicker copper pads that provided a means of stepping down in size from the power supply wire to 30 awg copper wire that was then soldered to the sample copper pads. This allowed for the sample to be handled without delamination of the sample copper pads and lines.

Another issue involved flow leakage from the sample during experimental testing. At high heat fluxes and flowrates, high sample inlet pressures were encountered. It should be noted that, from pressure testing, samples were found to fail at pressures nearing 300 kPa. Accordingly, inlet pressures were monitored in order to avoid sample failure, limiting the flowrate and heat flux ranges of the experimental tests. However, due to the inconsistency in the bonding of the clear cover from sample to sample, leaks developed, typically at the edges of the sample. Figure 2.1.7 displays an example of a leak during testing.

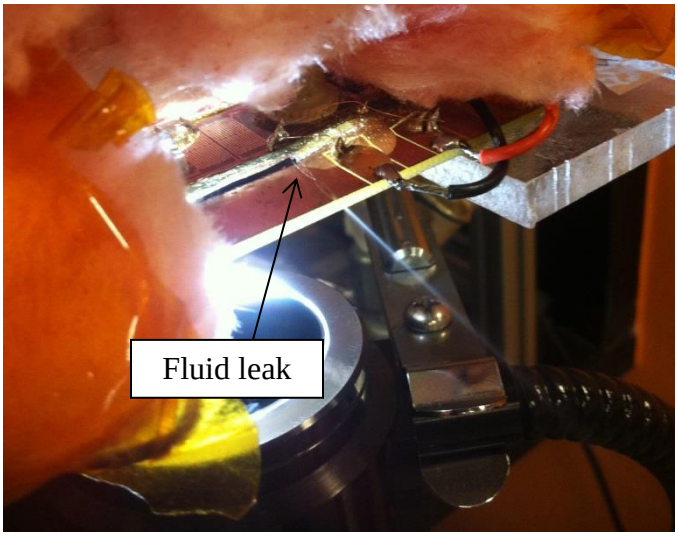

Figure 2.1.7 Image of sample leakage

2.2 Experimental Setup

For a test platform, a refrigerant flow loop was constructed to measure flowrate and the temperature rise and pressure drop across the heated pin fin sample, as can be seen in Figure 2.2.1. This setup consists of a primary refrigerant loop and secondary cooling loop. The primary loop is composed of a pump, flowmeter, two heat exchangers, metering valve and a pre-heater connected with insulated ¼" copper tubing. The secondary loop simply supplied chilled water to the backside of the copper heat exchangers. A schematic of the basic layout of the platform is shown in Figure 2.2.2.

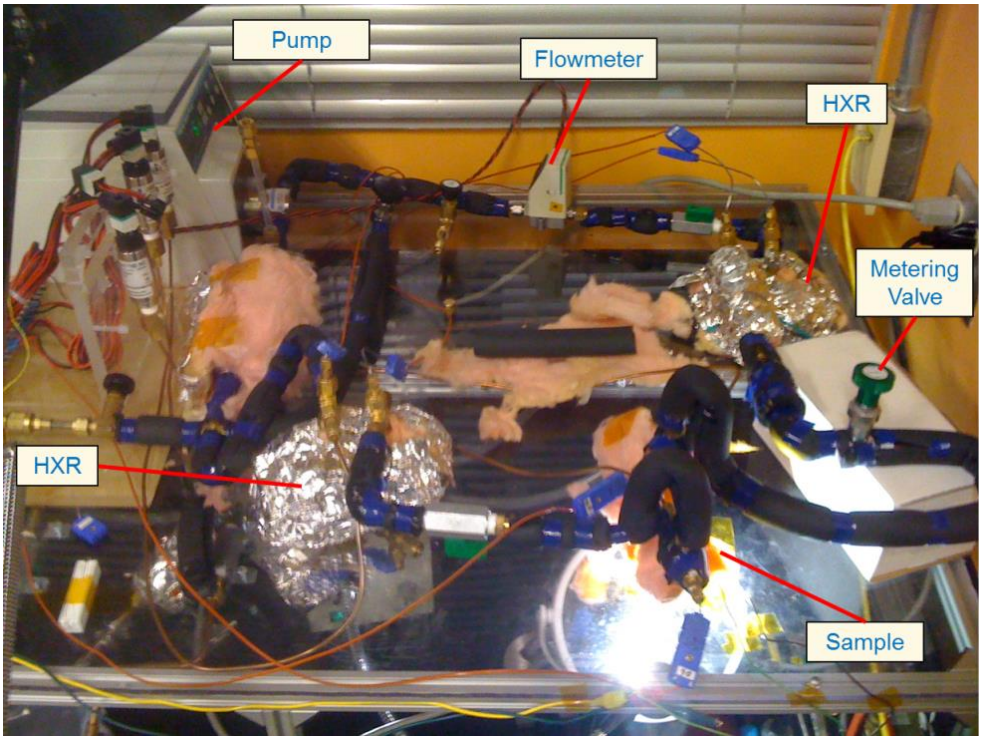

Figure 2.2.1 Closed flow loop platform

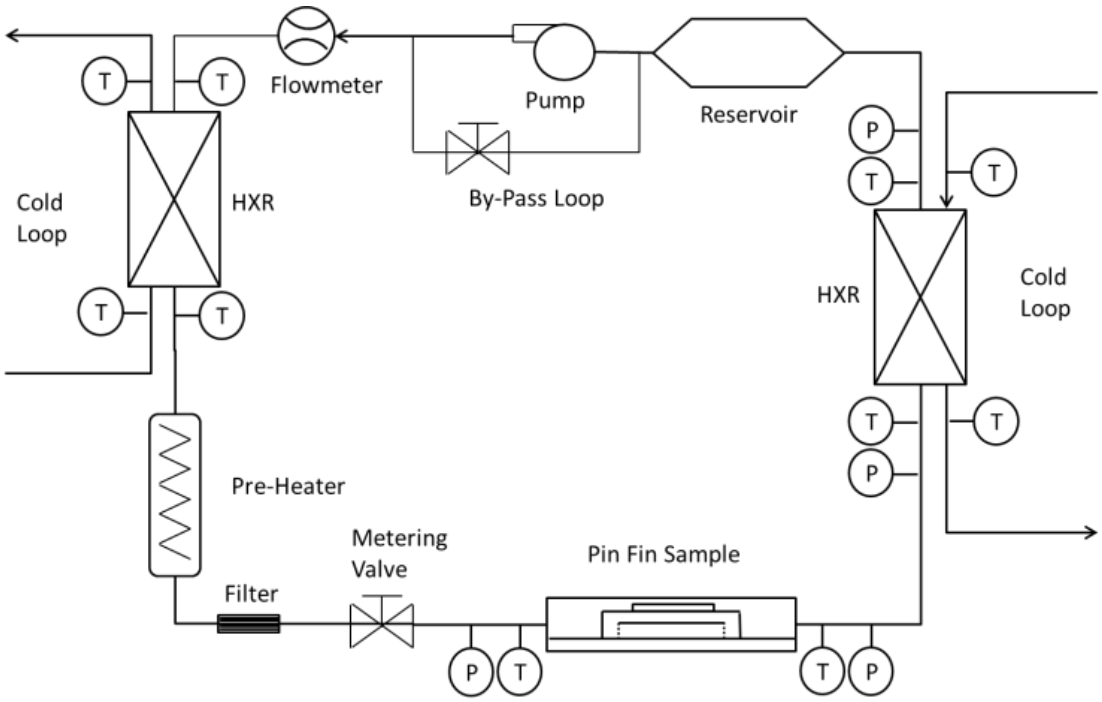

Figure 2.2.2 Closed flow loop schematic

A Cole-Palmer digital magnetic gear pump forced fluid through a 15μm pore-sized Swagelok inline filter. A McMillan, microturbine flowmeter with a 20 to 200 ml/min measurement range measured flowrate. The fluid then made its way through a copper heat exchanger was built by machining channels and inlet/outlet manifolds in a copper block that was then sealed with a plexiglass cover and o-ring. This heat exchanger assisted in the heat removal upstream of the pre-heater which was constructed by wrapping non-conductive tape around the copper tubing. The pre-heater allowed for control of subcooling into the sample. Fluid was then directed through a throttling valve before entering the pin fin sample. Pressure and temperature measurements were taken across the combination of sample and inlet/outlet tubing and fittings. These were the closest measurements points to the array since sensors were not fabricated in the samples. The pin fin sample was connected to the refrigerant loop via clear vinyl tubing. Insulation

was wrapped around the sample and clear tubing. Small sections of the tubing directly before and after the inlet/outlet ports were exposed to serve as viewing windows of the flow before and after the pin fin sample. The flowmeter, thermocouples and pressure transducers were connected to an Agilent data aquisition unit. With the sample facing down, a Photron high speed camera was placed directly below supported by a rigid stand (Figure 2.2.3). An annular light source between the camera and sample provided light for flow visualization data acquisition. Image capture ranged from 100-3000 fps (frames per second). Figure 2.2.4 shows the flow visualization setup.

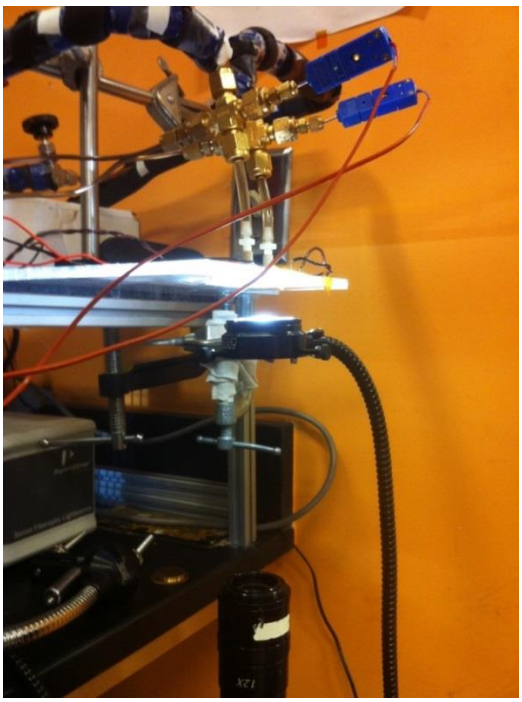

Figure 2.2.3 Flow visualization setup

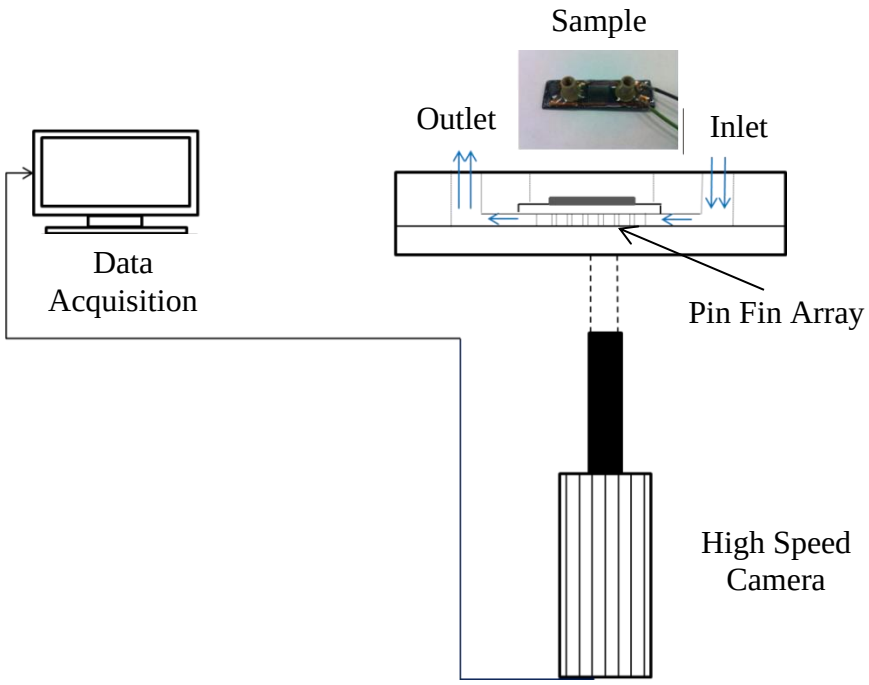

Figure 2.2.4 Flow visualization schematic

2.3 Experimental Procedure

Once a sample was connected to the flow loop, a vacuum pump was used to pull the system pressure down <2kPa. Then, a filling tank containing the R245fa working fluid was attached to the filling port of the loop. The filling loop valve was then opened, allowing the refrigerant to fill the system up to the pressure of the filling tank. The gear pump was started and the remaining required working fluid amount was allowed to fill the system. All tubing in the flow loop was insulated with 0.635cm insulation. All components, including the samples, were insulated with fiberglass insulation.

To begin the experimental runs, the system pump was used to run refrigerant R245fa through the primary loop, and chilled water was run through the secondary loop side of the heat exchangers. The metering valve and pre-heater located directly upstream

of the pin fin sample allowed for inlet pressure control and manipulation of subcooling conditions. The system was allowed to set until steady state conditions were reached. To initiate boiling, the flowrate was reduced to 5ml/min. The heater power was gradually raised in small increments until flow boiling could be seen (~20W/cm^2). After this, the flowrate and heater power were set to values corresponding to desired test values. Table 2.3.1 shows an example of the test matrix used during the experiments.

Table 2.3.1 Experimental test matrix

	20W	25W	30W	35W
20mlpm	h, x, flow	h, x, flow	h, x, flow	h, x, flow
25mlpm	h, x, flow	h, x, flow	h, x, flow	h, x, flow
30mlpm	h, x, flow	h, x, flow	h, x, flow	h, x, flow
35mlpm	h, x, flow	h, x, flow	h, x, flow	h, x, flow
40mlpm	h, x, flow	h, x, flow	h, x, flow	h, x, flow

One baseline test conducted was to quantify the heat added to the pin fin array, during an active test, due to the heat from the flow visualization light source. To evaluate this, the flow loop with the pin fin sample installed was run. With a flowrate of 10ml/min the light source was dialed to its highest power and the system was allowed to reach steady state (<0.5^{o}C change in thermocouple readings). For each sample, this procedure was conducted and the result was a temperature rise across the array less than 0.5^{o}C, indicating a negligible heat input from the visualization light source.

2.4 Data Reduction

Power input to the embedded heaters was calculated from current and voltage measurements according to:

$$\boldsymbol{q_{total} = IV} \tag{3.1}$$

The heat flux into the pin fin array was calculated from:

$$\boldsymbol{q_{eff} = \dot{m}(h_{out} - h_{in})} \tag{3.2}$$

using temperature measurements across the sample. Performing a single phase study and using the above equations provided a means of calculating heat loss from the pin fin array. Initial single phase measurements indicated an 8% heat loss from the array. This value was used for subsequent two-phase calculations.

For each case, an average *h* was calculated using the fin efficiency model [28]. The area of the base of the pin fin array was:

$$\boldsymbol{A_b = {L_b}^2} \tag{3.3}$$

and the area of the base exposed to the fluid was:

$$\boldsymbol{A_{e,b} = A_b - NA_{c,fin}} \tag{3.4}$$

where *N* was the number of fins. To find the total area of the fins exposed to the fluid:

$$\boldsymbol{A_{e,fin} = NP_f L_f} \tag{3.5}$$

Due to the fabrication of the pin fin sample, the contact between the glass cover and fin tip could not be guaranteed. In other words, it is possible that a gap between the fin tips and glass cover exists, thus introducing an active tip condition to the analysis. It has been shown, however, that use of the adiabatic tip analysis can predict, approximately, the results of a fin with an active tip as long as the fin length is corrected to account for heat loss through the fin tip. Accordingly, a corrected fin length commonly used for pin fins was introduced as:

$$\boldsymbol{L_{f,corr} = L_f + D/4} \tag{3.6}$$

Where L_f was the actual length of the fin. Assuming a fin under an adiabatic tip condition, the fin efficiency was expressed as:

$$\boldsymbol{\eta = \frac{\tanh(mL_{f,corr})}{mL_{f,corr}}} \tag{3.7}$$

where:

$$\boldsymbol{m = \sqrt{\frac{hP}{kA_{c,fin}}}} \tag{3.8}$$

The effective power into the fluid stream over the array can then be expressed as:

$$\boldsymbol{q_{eff} = h(A_{e,b} + N\eta A_{e,fin})(T_w - T_\infty)} \tag{3.9}$$

where T_∞ is the average fluid temperature or saturation temperature depending on the type of phase condition occurring across the pin fin array (single or two-phase). For two-phase flow, saturation temperature was calculated based on pressure drop across the array and working fluid properties. Between the inlet and outlet pressure measurements a linear

pressure drop was assumed over the sample. The pressure drops through the clear tubing and 90^{o} passages of the sample were calculated and were negligible compared to that across the pin fins. The average pressure over the sample was used for determining saturation temperature. The base temperature, T_w, was calculated using the linear resistance vs. temperature relationship of the sample's Pt heaters. Each heater was calibrated using a temperature controlled oven to determine the temperature coefficient, α. During testing, base temperatures were calculated by using the linear relationship:

$$\boldsymbol{R(T) = R_o(1 + \alpha \Delta T)} \tag{3.10}$$

where R is the heater resistance and R_o is the reference heater resistance measured at ambient temperature. The temperature coefficient ranged from 0.00281/^{o}C to 0.00332/^{o}C for the different heaters used in the study.

From here, an iterative approach was used to obtain the average or local heat transfer coefficient depending on size and location of the heater (Figure 2.4.1). A thermodynamic calculation was used to determine vapor quality. Exit enthalpy was calculated from:

$$\boldsymbol{q_{eff} = \dot{m}(h_{out} - h_{in})} \tag{3.11}$$

where q_{eff} was the heat into the stream after considering heat loss from the sample. Since this study considers only inlet subcooling, inlet enthalpy was calculated as the fluid enthalpy at the inlet temperature. Vapor quality at the array outlet was then calculated by:

$$\boldsymbol{x = (h_{out} - h_{f_{out}}) \,/\, (h_{g_{out}} - h_{f_{out}})} \tag{3.12}$$

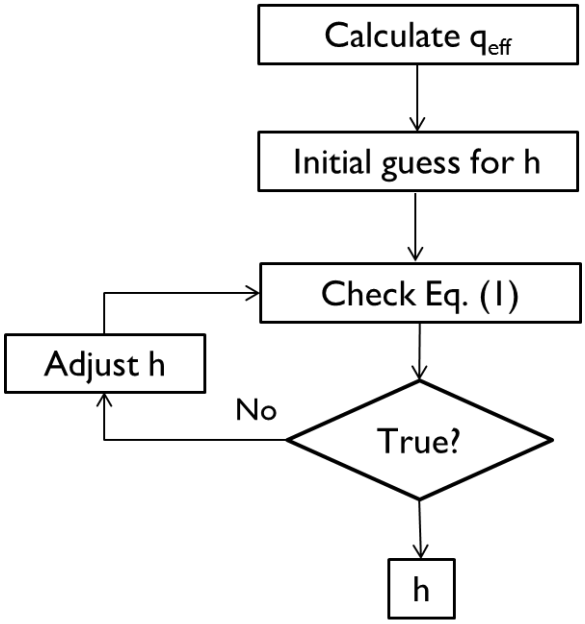

Figure 2.4.1 Data reduction method

2.5 Uncertainty Analysis

Table 1 shows uncertainties of experimental measurements. Propagation of uncertainty analysis was used to determine uncertainty of calculated results.

Table 2.5.1 Experimental uncertainties

Quantity	± **Uncertainty**
I/O temperature, T (^{o}C)	0.5 ^{o}C
I/O pressure, (kPa)	0.25%
Mass flux, G (kg/m^{2}s)	3%
Current, I (A)	0.1%
Voltage, V (V)	2.6%
Heater Power (W)	2.6%
Fin height (μm)	3%
Sample length, L (cm)	2%
Sample width, w (cm)	2%
Heat transfer coefficient, h (W/m^{2}K)	10-20%

CHAPTER 3

RESULTS

3.1 Uniform Heating

For this study, twenty different cases were run at various heater powers and flow rates. The inlet port viewing window was monitored to ensure that a subcooled condition was maintained. For each case, the system was allowed to reach a steady state, which took roughly 5 minutes. Subsequently, data was collected at 1Hz. An average was obtained over these data points to get final measured values. Video of flow boiling over the sample was also taken. Selected parameters are shown in Table 3.1.1.

Table 3.1.1 Uniform heating parameters

Parameter	**Range**
Heat flux (W/cm^2)	20-35
Flowrate (ml/min)	20-40
Subcool (^oC)	15-20
Inlet pressure (kPa)	183-230
Pressure drop (kPa)	33-67

A few interesting trends can be seen from Figures 3.1.1 and 3.1.2. Heat flux error bars have been omitted but maximum values are reported in Section 2.5. As heat flux is increased to the pin fin sample, the average *h* decreases. Also, the average *h* decreases with increasing vapor quality. This result was unexpected with the anticipation that *h* would improve with the introduction of flow boiling over the array. This trend was also

recognized by Qu and Abel [23] for pin fin geometry and Agostini et al. [29], [30] in the case of microchannel devices.

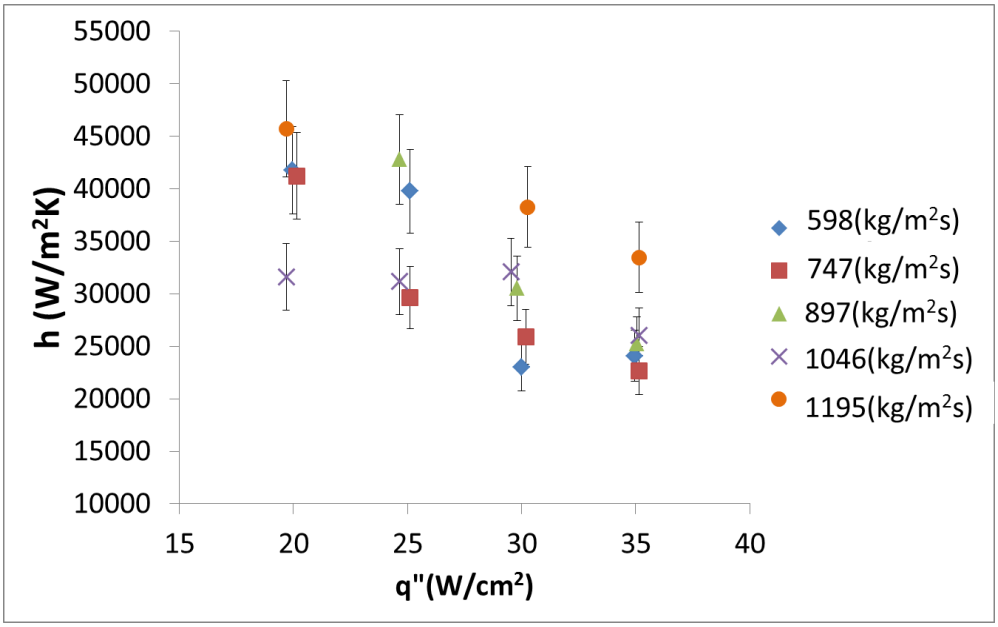

Figure 3.1.1 *h* vs. *q"*

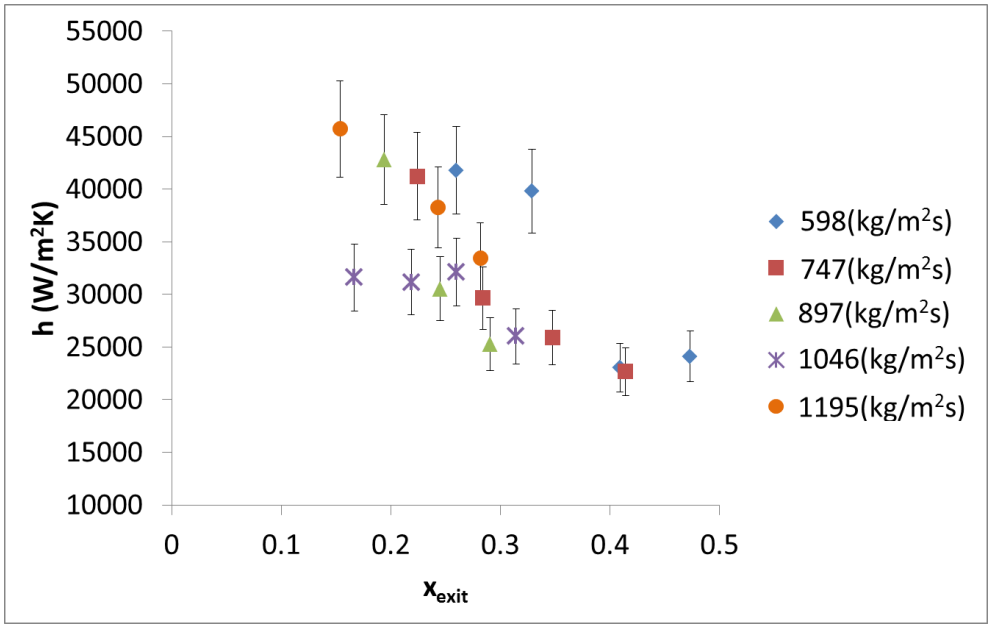

Figure 3.1.2 *h* vs. x_{exit}

Previous studies have identified two types of flow regimes commonly associated with this type of internal flow. At low qualities, the bubbly flow regime is dominant and is linked to the nucleate flow boiling mechanism. In this region, vapor bubbles grow and detach from bubble departure sites on the heated surface and are small relative to the hydraulic diameter of the passage. Heat transfer is achieved through phase change at the bubble departure sites and high local *h*. High local *h* is a result of increased mixing near the heated area due to bubble growth and detachment. In this regime *h* is a strong function of heat flux and is less dependent on mass flowrate. At higher qualities, the annular flow regime is dominant and is linked to the convective flow boiling mechanism. Heat transfer is achieved by conduction through the liquid film and evaporation at vapor/liquid interface. In this regime, *h* is a strong function of mass flowrate and less dependent on heat flux. Typically, an increasing *h* trend occurs with increasing heat flux until a maximum value is reached, after which *h* decreases monotonically. For this study, however, only a decrease in *h* is detected.

From Figures 3.1.3 and 3.1.4, two separate sections, liquid and liquid/vapor mixture, are apparent on the samples. Bubble departure begins towards the middle of the pin fin array for high heat loads and low flowrates, with large, triangle-shaped liquid/vapor wakes covering a large portion of the downstream portion of the array. For increasing flowrates and decreasing heat loads these bubble departure points migrate towards the back of the sample. The two-phase front also moves as the wakes behind these bubble departure points decreases in size. The migration of the two-phase front had a much stronger dependence on heat flux then it did with flowrate. This interesting wake structure demonstrates the two-dimensional spreading of vapor bubbles around the pin

fins and suggests that pin fin enhancement also provides a flow distribution advantage when compared to more constrained geometries like microchannels. A major disadvantage of two-phase flow in microchannels is reverse flow upstream due to vapor expansion within the channel.

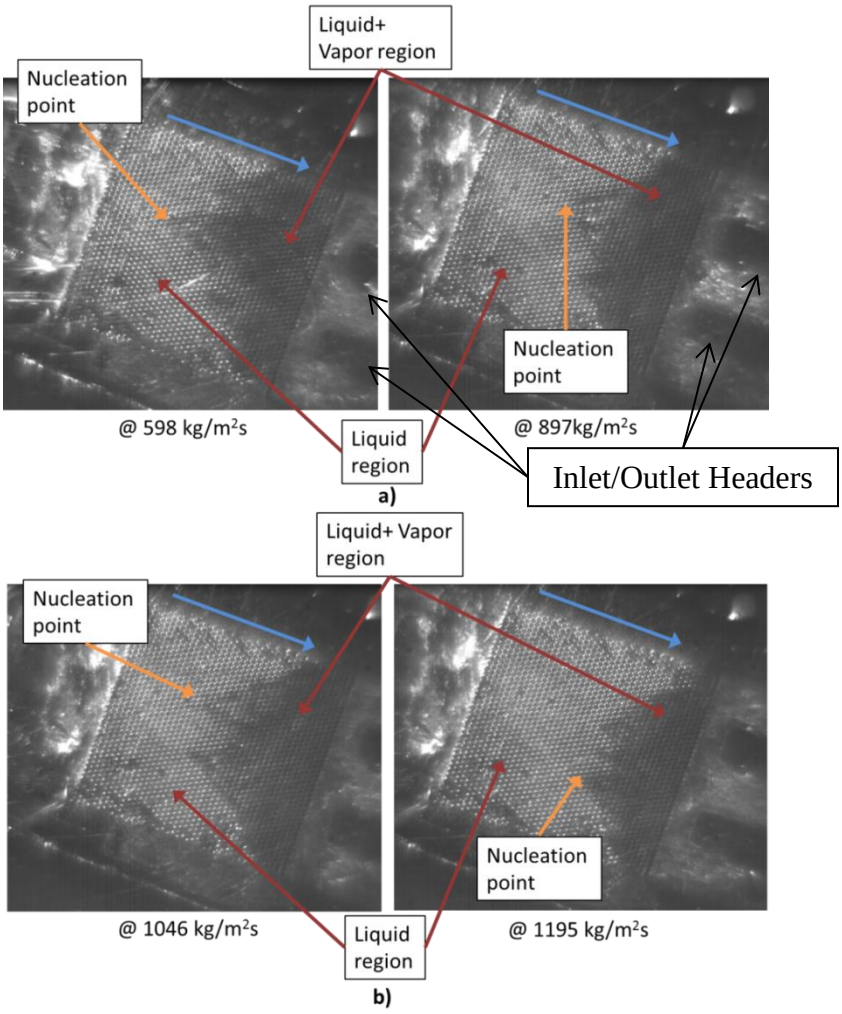

Figure 3.1.3 Flow visualization with q" = 30 W/cm^2 at a) G = 598 and 897 kg/m^{2}s and b) G = 1046 and 1195 kg/m^{2}s

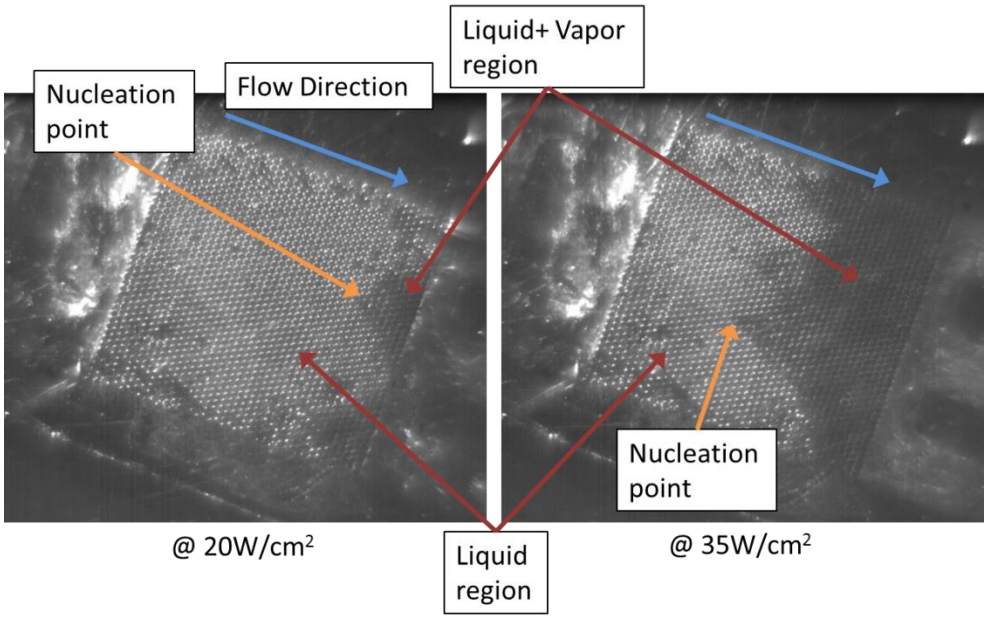

Figure 3.1.4 Flow visualization at G = 1046 kg/m^{2}s

The conical features of the vapor wakes are attributed to the inherent 2D geometry of the pin fin micro-gap, allowing for lateral pressure distribution and vapor spreading behind bubble departure points. Similar trends were observed for all experiments. Figures 3.1.5 and 3.1.6 show the current data compared with data of Kosar and Peles [31] in which a hydro-foil based pin fin device is tested using R-123 working fluid. By observation of Figure 3.1.5, the decreasing trend of the current study occurs at lower heat fluxes suggesting an earlier transition to boiling than R-123 working fluid. This is justified since the boiling point of R-245fa is 12^{o}C less than R-123 at constant pressure and boiling would occur at lower heat fluxes. Here, *h* as a function of vapor quality is in reasonable agreement, as indicated by Figure 3.1.6. Due to the pressure limit of the sample the flowrate and heat flux ranges were limited. Without data over larger parameter ranges, it is postulated that the current data is possibly part of a larger "m-curve" that only captures

the decreasing trend after the maximum *h* value. A slightly broader range of parameters is used for the partial heating study.

In order to explain the *h* characteristics observed during the study, dominant heat transfer mechanisms for each type of internal, flow boiling regime were considered. For the single-phase region, heat is transferred by convection from the sample base and pin fins to the liquid. For nucleate boiling, heat transfer is dominated by continuous wetting of the surface by liquid for bubbly flow while heat transfer to vapor occurs when bubbles coalesce. Annular flow begins as a liquid film covering the pin fins and base but eventually forms dry areas (dry-out) for increasing heat flux . These dry areas constitute a drop in *h* since the thermal conductivity of vapor is significantly less than liquid.

Qu and Siu-Ho [23] identified annular flow as the dominant flow regime in pin fin enhanced gaps with liquid film covering the pin fin surfaces and considered to be sustained by a balance between deposition of discrete droplets entrained in the vapor core and evaporation of the liquid film. For the current study, one can develop a reasonable explanation for the heat transfer trends. For high flowrates and low heat fluxes the flow map shows small triangle-shaped vapor wakes towards the end of the sample. When the heat flux is increased the vapor wakes increase in size, thus increasing vapor quality and covering a larger area of the pin fin sample. The fact that *h* values drop coincides with an assumption that the majority of liquid/vapor region is not experiencing nucleate boiling and, instead, is dominated by convective flow boiling or partial and intermittent dry-out where *h* is known to decrease.

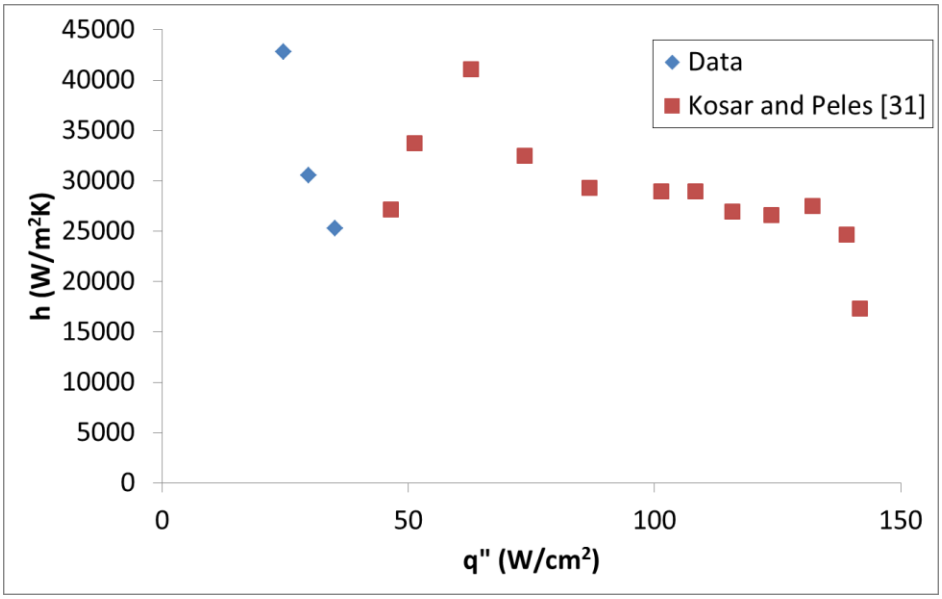

Figure 3.1.5 Heat transfer coefficient vs. heat flux for current data (G=897kg/m^{2}s) and Kosar and Peles [31] (G=976kg/m^{2}s)

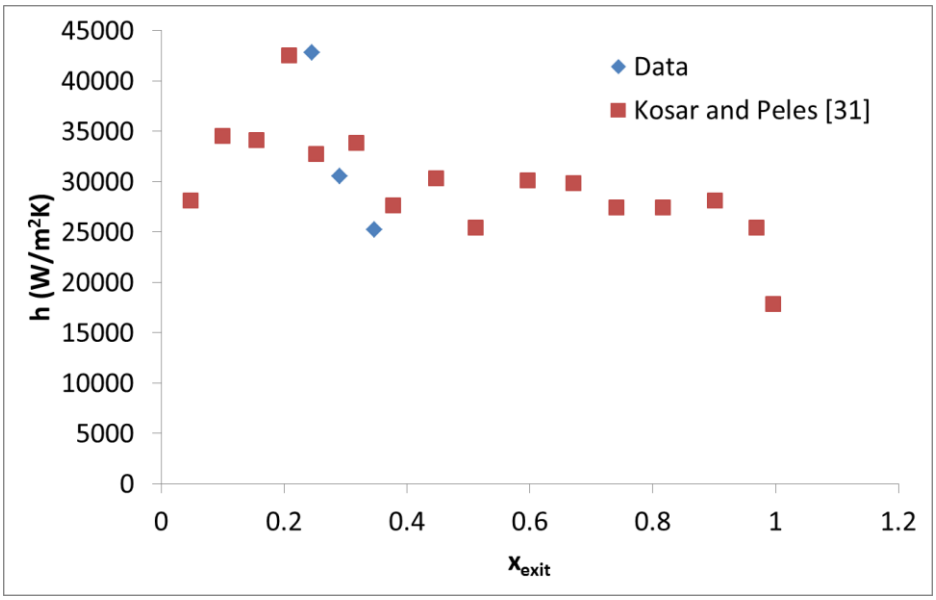

Figure 3.1.6 Heat transfer coefficient vs. exit vapor quality for current data (G=897kg/m^{2}s) and Kosar and Peles [31] (G=976kg/m^{2}s)

To further investigate the dominant flow boiling mechanism flow regime mapping is used. The superficial liquid and vapor velocities were calculated for the study. These points were plotted in Figure 3.1.7 and compared with the flow transition defined empirically by a study considering similar device geometry and working fluid. The dashed line displays the transition between wavy intermittent and spray-annular as defined by the authors. The data from the current study fall within the spray-annular region. The current data was also used to calculate the nondimensional parameters used for the theoretical flow regime mapping.

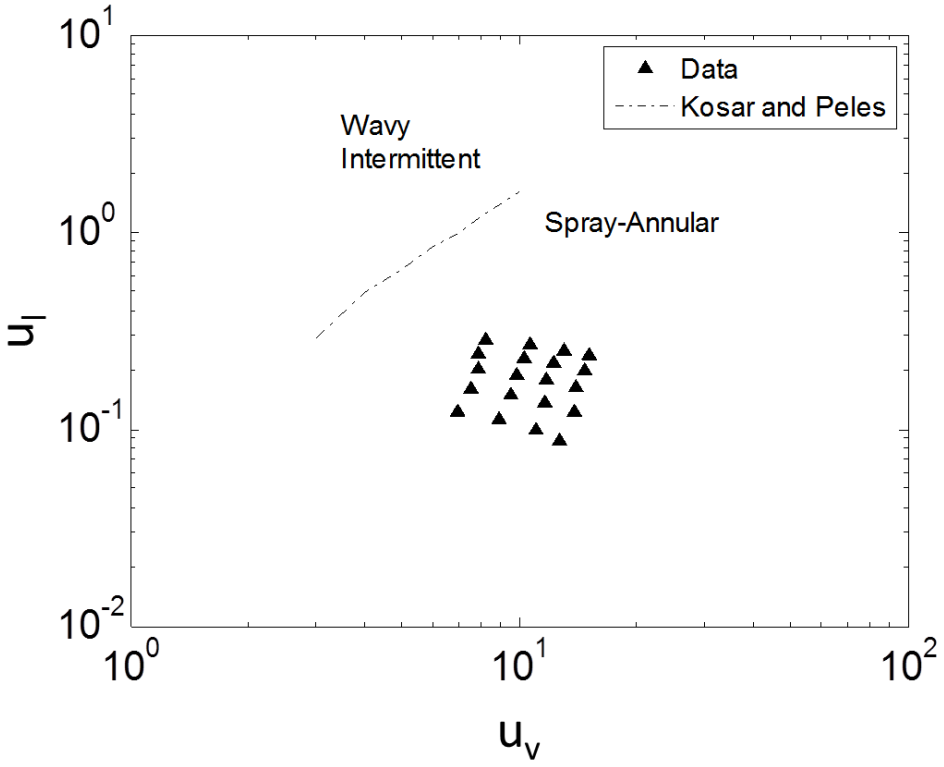

Figure 3.1.7 Flow map indicating relation to experimental flow regime transition of Kosar and Peles [31]

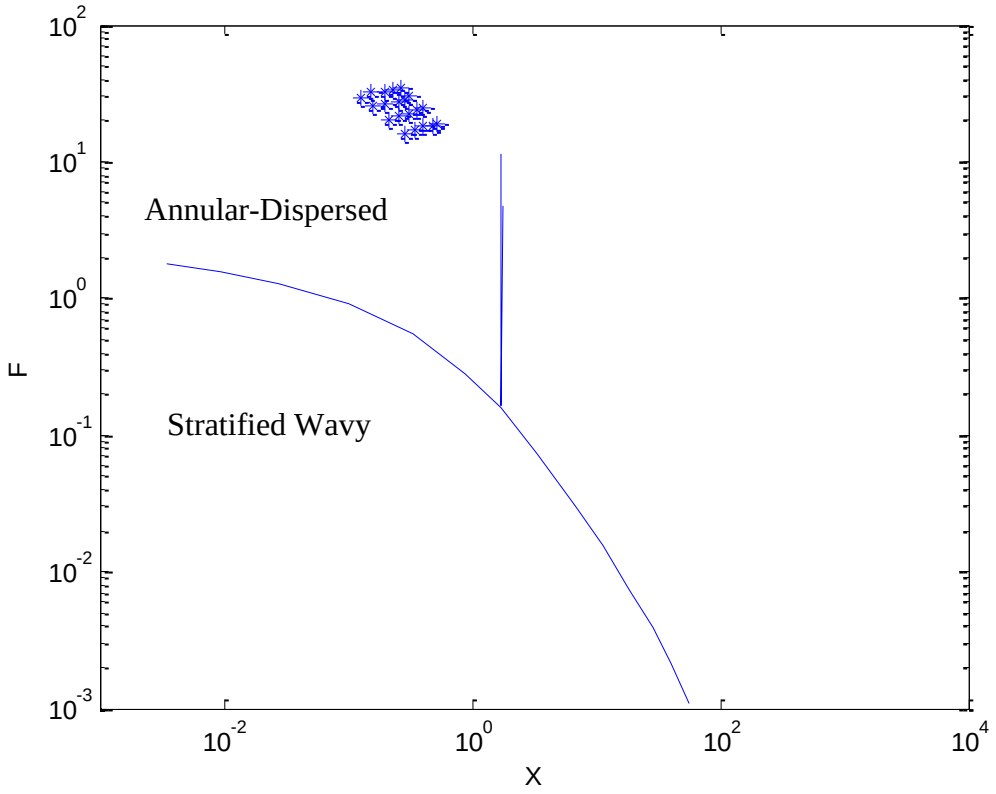

Figure 3.1.8 Data plotted on Taitel-Dukler flow regime map

Figure 3.1.8 shows the current data plotted on a Taitel-Dukler regime map. The data falls within the Annular-Dispersed region. Since the convective boiling mechanism is associated with the annular regime this helps to validate the proposed flow pattern and boiling mechanism.

A few interesting observations concerning the physical characteristics of the two-phase flow inception and interaction with the array were seen. Figure 3.1.9 displays the progress of the two-phase wake downstream of the bubble departure point. As noted previously, location of bubble departure points depend on the applied heat flux to the array with further upstream locations coinciding with higher heat fluxes. A study at 1000

fps reveals that the conically shaped vapor wakes are actually a result of a rapid, periodic cycle of vapor slug vaporization. Bubble departure begins at a single point with a single bubble growing, detaching and traveling downstream due to initial forces. Shortly after detachment, the bubble undergoes rapid vaporization, expanding into a large, vapor slug covering a majority of the wake region.

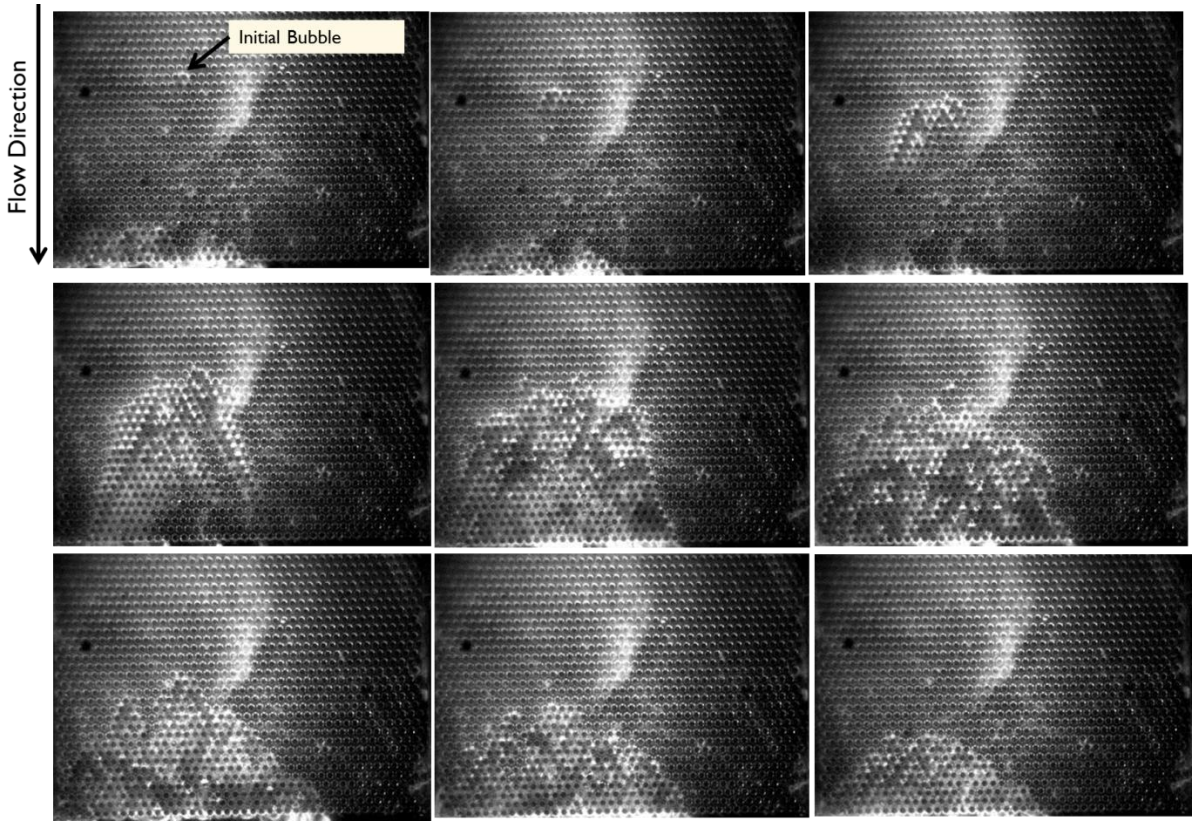

Figure 3.1.9 Development of two-phase wake downstream of bubble departure point

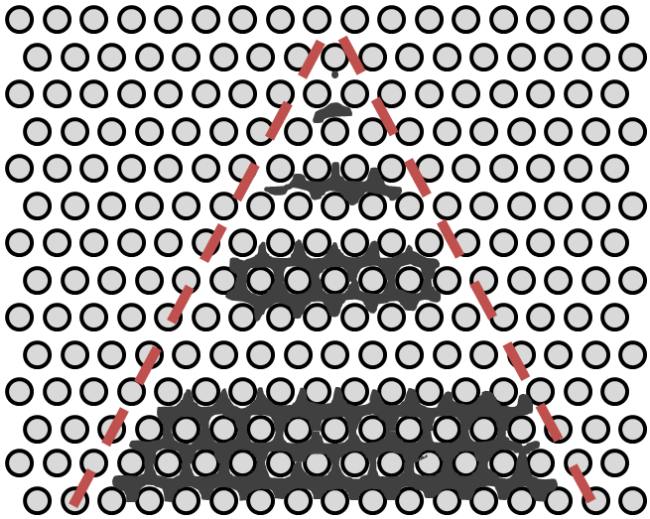

Figure 3.1.10 Diagram demonstrating conical shape of vapor wake

Eventually, the vapor slug exits the array at which point the periodic, vapor wake process repeats. Thus, the region downstream of the bubble departure point is exposed to a sequence of vapor and liquid slugs. A similar vapor slug sequence was demonstrated by Krishnamurthy and Peles [32]. The reasoning for this periodic vapor pulsing has yet to be confirmed. One possible source of this affect was the operation and control of the sample heaters. The basis of the power supply control was control current where voltage drop depended on electrical resistance of the heater and electrical leads. Due to platinum's strong dependence of electrical resistance on temperature the resistance of each heater varied for changes in array base temperatures. Thus, voltage from the power supply would be automatically modulated for changes in base temperature. Large changes in base temperature would be expected due to changes in thermal resistance in response to an alternate existence of pure liquid and two-phase conditions in the two-phase wake regions of the array. It is possible that these rapid and period vapor burst are a consequence of the power modulation of the power supply. A more detailed investigation

including power and local temperature fluctuations must be performed to validate this hypothesis.

For the same experimental parameters, locations of all bubble departure points were not consistent from one test to the next. If, for example, bubble departure points developed at particular pins or positions along the array base for one experimental run, the next run did not result in the same bubble departure points as the first. However, some points along the array were consistent from run to run. Therefore, it was important to investigate where these bubble departure points developed, and identify any geometrical features that may promote bubble departure along the array. Two different geometrical features were identified where bubble departure occurred. Some bubble departure points developed at the surface of various pins. Vapor bubbles developed typically between 90^o and 180^o along the pin fin surface, shifted to the downstream portion of the pin fin surface, and grew to 50-75μm in diameter before detaching and traveling downstream.

Figure 3.1.11 displays one example of vapor bubble departure, growth and detachment at the pin surface. This behavior of bubble growth and detachment can be explained based on basic flow around a single pin. The region of lowest pressure around the surface of a cylinder is located at 90^o from the stagnation point. This low local pressure coincides with lower saturation temperature allowing vapor bubble departure at lower surface temperature. Once the vapor bubble forms it is forced around the pin due to shear stress and inertial forces. The vapor bubble stops at 180^o in the region of recirculation and grows to 50-75μm before detaching from the pin surface. These areas of recirculation (vortices) in microscale pin fin arrays were reported by Renfer et al [33]. The particular pins in which bubble departure occurred varied.

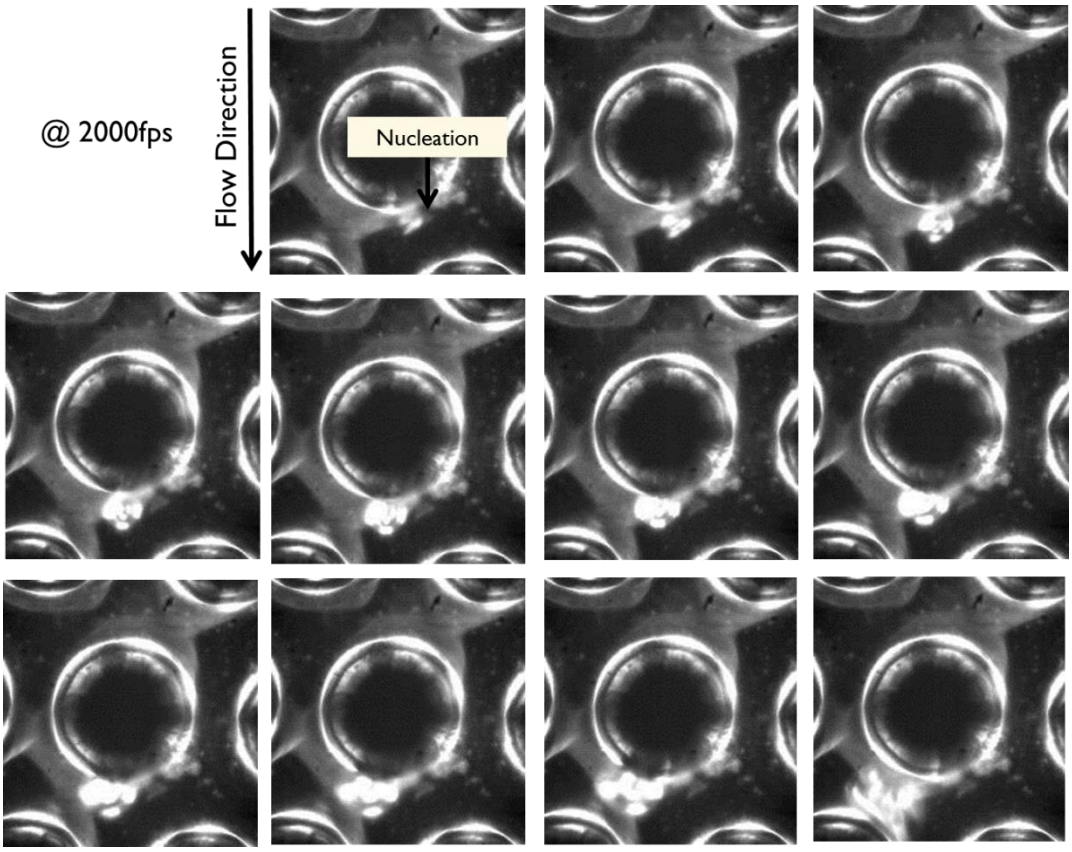

Figure 3.1.11 bubble departure at pin surface

This was not only dependent on the specific experimental run, but also on the experimental parameters, particularly dependent on heat flux. For lower heat fluxes, bubble departure points formed at downstream locations of the array. For increasing heat flux bubble departure points progressively shifted to upstream pins. As mentioned, there were some locations that had consistent vapor bubble departure. From high magnification visualization it was determined that these locations contained surface defects. Figure 3.1.12 shows one such defect with vapor bubble departure. It is believed that a microscale scratch exits along the base of the array due to fabrication processes and device handling. Vapor bubble departure occurs near the center of the scratch and is consistent throughout experimental runs. It has been well documented that surface roughness features such as

scratches or cavities promote vapor entrapment [34]. At the interface of the liquid and these entrapped vapor regions vaporization takes place, allowing a bubble departure site to develop at a lower temperature compared to the relatively smooth surrounding surface of the array base. Thus, these sites would require less superheat to trigger bubble nucleation and departure and would appear at lower applied heat flux.

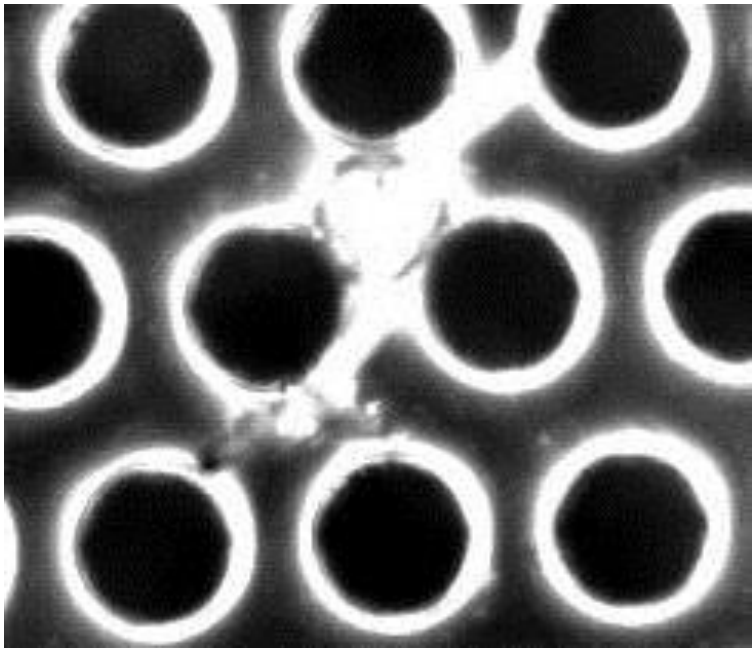

Figure 3.1.12 bubble departure at base defect

With all results indicating a decreasing *h* and, therefore, possible intermittent dry-out, a higher magnification visualization study was performed in order to evaluate what was occurring physically near the pin surface downstream of bubble departure points. In the flow visualization process the pin fin array was divided into 675μm x 2925μm sections and image capture was executed at a rate of 3000 fps for each section. Each section contained roughly 4 rows of pins, and images were taken along the array from the

upstream to the downstream so that, after imaging was complete, the sections could be pieced together to represent the flow boiling process spanning the length of the array.

An important characteristic of vapor flow over the pin fins was the existence of a liquid film at the surface. If a liquid film was present on the pin fin surface heat transfer was achieved by conduction through the film and evaporation at the liquid/vapor interface. If the pin fin surface was in contact with vapor, heat transfer was achieved by convection and conduction with vapor. For R245fa the thermal conductivity of liquid is 8x greater than vapor. Hence, the heat transfer performance of the device hinges on the physical characteristics at the pin fin surface.

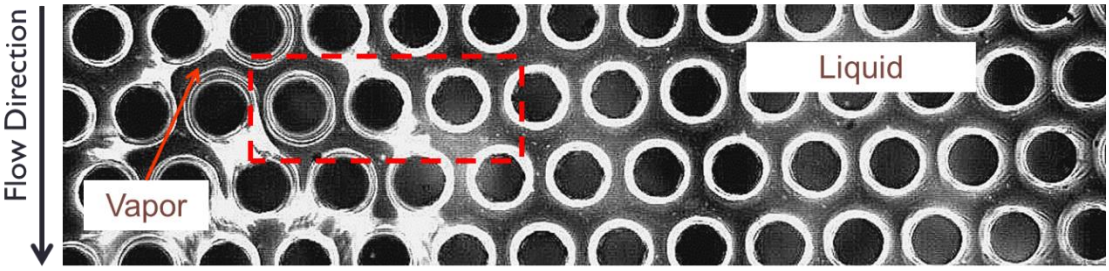

Figure 3.1.13 High magnification of two-phase region downstream of bubble departure site

Figure 3.1.13 displays a section of the two-phase region downstream of a bubble departure site with vapor and liquid regions designated. In an attempt to identify the physical characteristic at the pin fin surface in the vapor region, pins in both vapor and liquid regions were compared. The dashed line highlights three specific pins with the left and right pins located in the vapor and liquid regions, respectively. Though the pixel value at the surface of the pins differ, it is not possible to determine with certainty

whether a liquid film is present around the pin in the vapor region. The current visualization process relies on reflection of light at the liquid/vapor interface to distinguish between the phases. Reflection is also used to identify the periphery of individual pins. Therefore, at the pin surface in the vapor region, pixel value is dependent on reflection from both the pin surface and liquid/vapor interface.

3.2 Partial Heating

This case considered partial heating of the pin fin array. Only the upstream heaters were active as depicted in Figure 3.2.1.

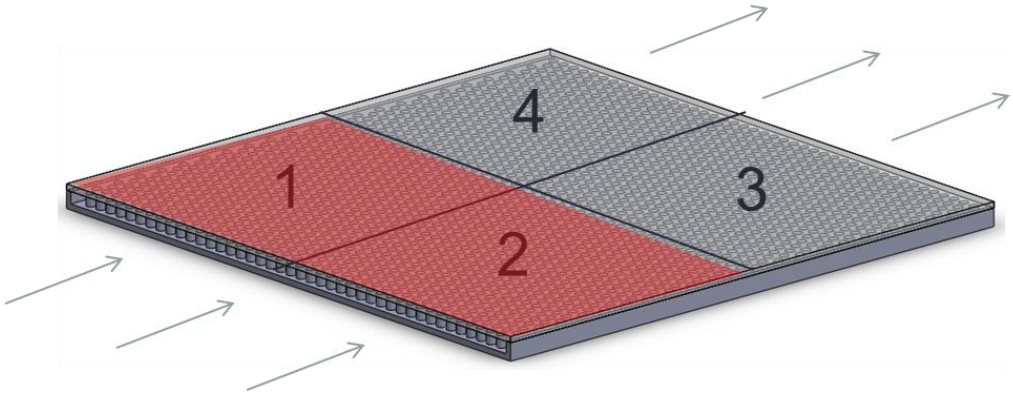

Figure 3.2.1 Diagram of partial heating using upstream heaters

Subcooling was between 10 and 13^{o}C for this study. Figure 3.2.2 displays average *h* with increasing heat flux. Single phase flow is identified via flow visualization at relatively low heat flux. In this region *h* decreases due to an increase in base temperature of the upstream heaters. This indicated that under single-phase conditions and for the flowrates considered flow was not fully developed. This same decrease in *h* (increase in total thermal resistance) is also reported in literature for a similar pin fin device under similar

single-phase conditions [17]. Near a heat flux of 19 W/cm^2 as heat flux is increased, a sharp jump in *h* is seen due to initiation of flow boiling over the array. A maximum value of 52,545 W/m^{2}K is reached. This is then followed by a steep decrease in *h*, eventually reaching a steady decline near 20,000 W/m^{2}K at 30 W/cm2.

Similar to Kosar and Peles [31], after reaching its maximum value, *h* decreases with increasing heat flux, which is attributed to the convective boiling mechanism. In literature, *h* gradually increases from single-phase up to the maximum value in this partial boiling region. In this study, however, a rapid jump in *h* is recorded from single to two-phase conditions over a relatively small heat flux change of 4W/cm^2. Immediately after this jump, the two-phase flow region is distributed as shown in the first image of Figure 3.2.4. It is determined that since *h* only decreases during the two-phase portion of the tests, the data suggests that the dominant flow boiling mechanism is convective flow boiling, while nucleate boiling associated with an increase in *h* for increasing heat flux is nonexistent. Figure 3.2.3 compares the two-phase data of the current study to the convective boiling correlation of Kosar and Peles [31]. This correlation is in reasonable agreement with the data with the largest discrepancy occurring at the initiation of two-phase flow.

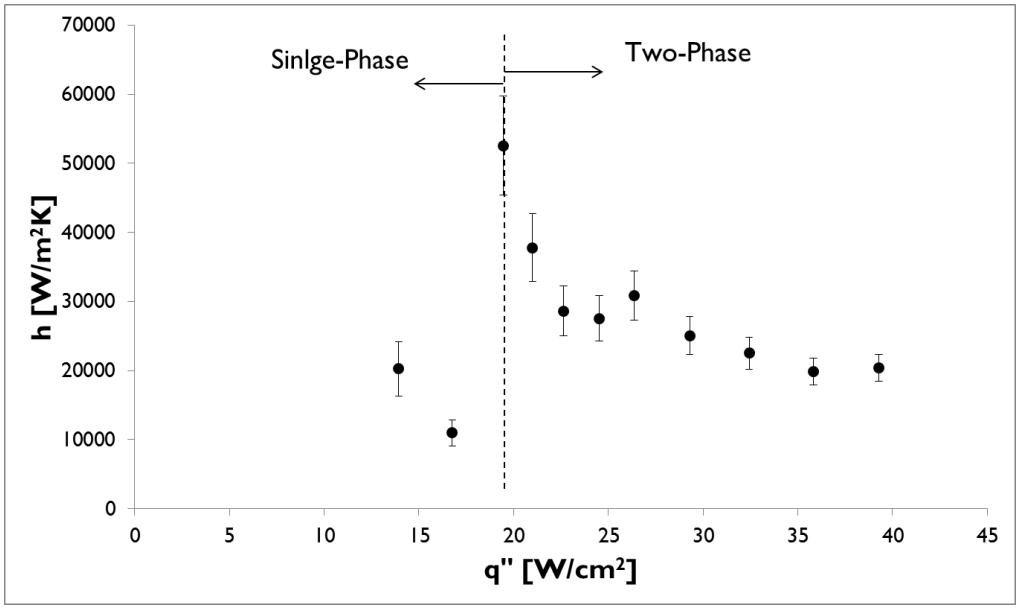

Figure 3.2.2 *h* vs. *q"* at G = 888 kg/m^{2}s

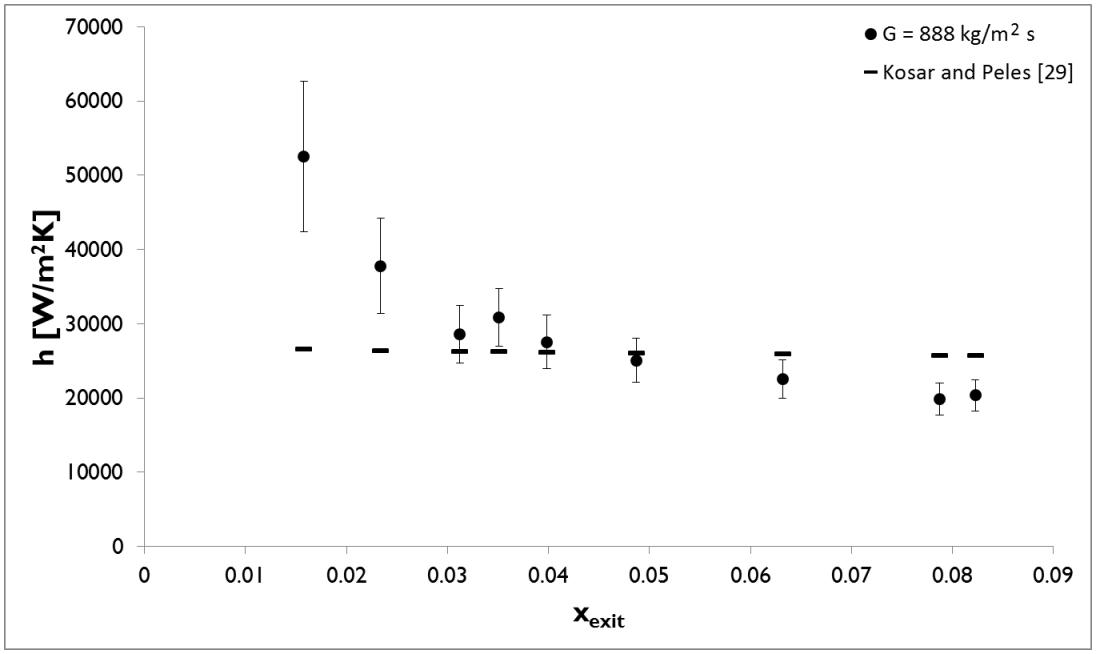

Figure 3.2.3 *h* vs. x_{exit} at G = 888 kg/m^{2}s

The first image of the flow visualization in Figure 3.2.4 indicates locations of heaters 1 and 2 (upstream heaters). Unlike the array area associated with heater 2, a large two-

phase region covers a majority of the heater 1 area. This is considered to be a consequence of surface roughness differences between these two areas since the power supplied to each heater is constant. A physical analysis of the surface roughness has yet to be performed. Conical-shaped wakes can be seen forming downstream of bubble departure points.

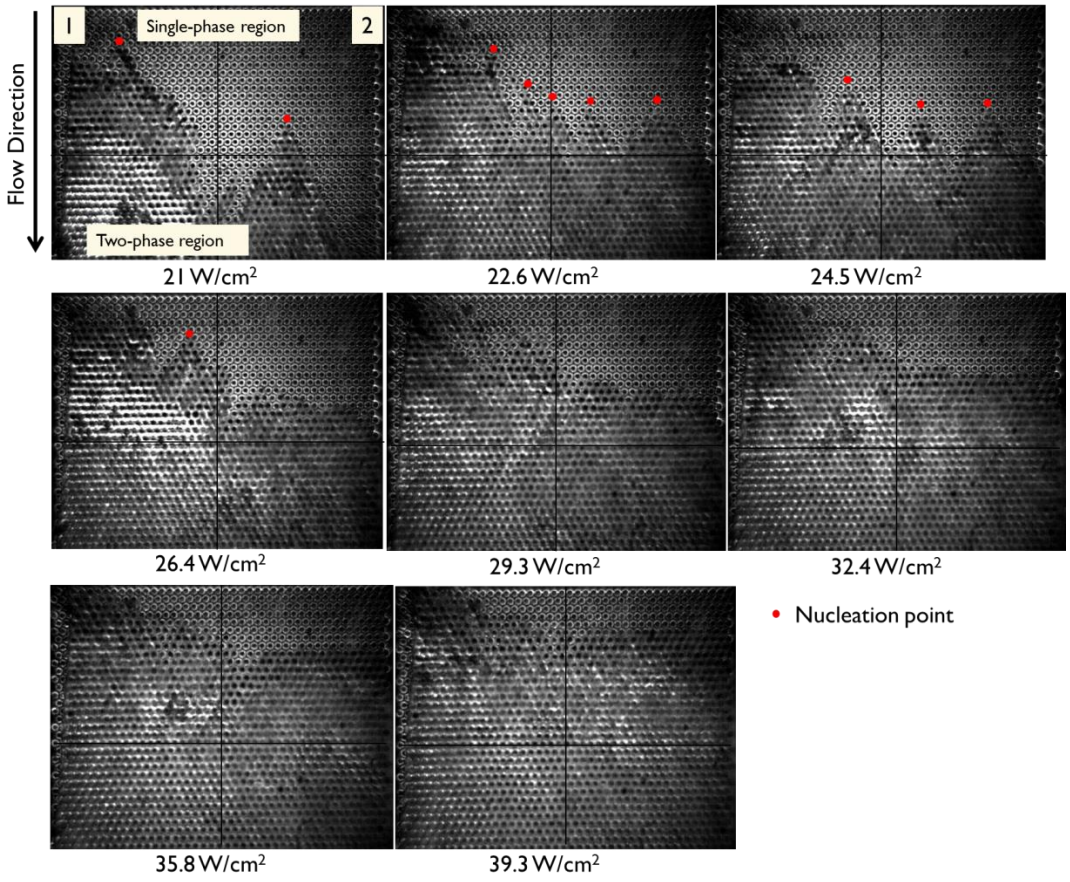

Figure 3.2.4 Flow visualization performed at a frame rate of 2000 fps

This demonstrates the two-dimensional spreading of flow, as is characteristic with this type of pin fin enhancement [35]. These unique wake structures continue to grow and merge until a majority of the array is blanketed by a two-phase region at 39.3 W/cm^2.

This is believed to be a consequence of conduction from the upstream heaters to the downstream base of the array for increasing heat flux.

In order to evaluate the dependence on flowrate, two-phase conditions were tested at various mass fluxes. Boiling was initiated at G = 300 kg/m^{2}s, at which point both heat flux and flowate were increased to the experimental parameters. Figures 3.2.5 and 3.2.6 show *h* dependence on heat flux and exit vapor quality, respectively. Error bars were omitted from Figure 3.2.6 for clarity. At flowrates of 1230 kg/m^{2}s and 1639 kg/m^{2}s *h* decreases before slightly increasing. At a flowrate of G = 888 kg/m2s the trend is a slight increase followed by a slight decrease. Despite the trends at individual flowrates, *h* tends to level out around 12,000 W/m^{2}K.

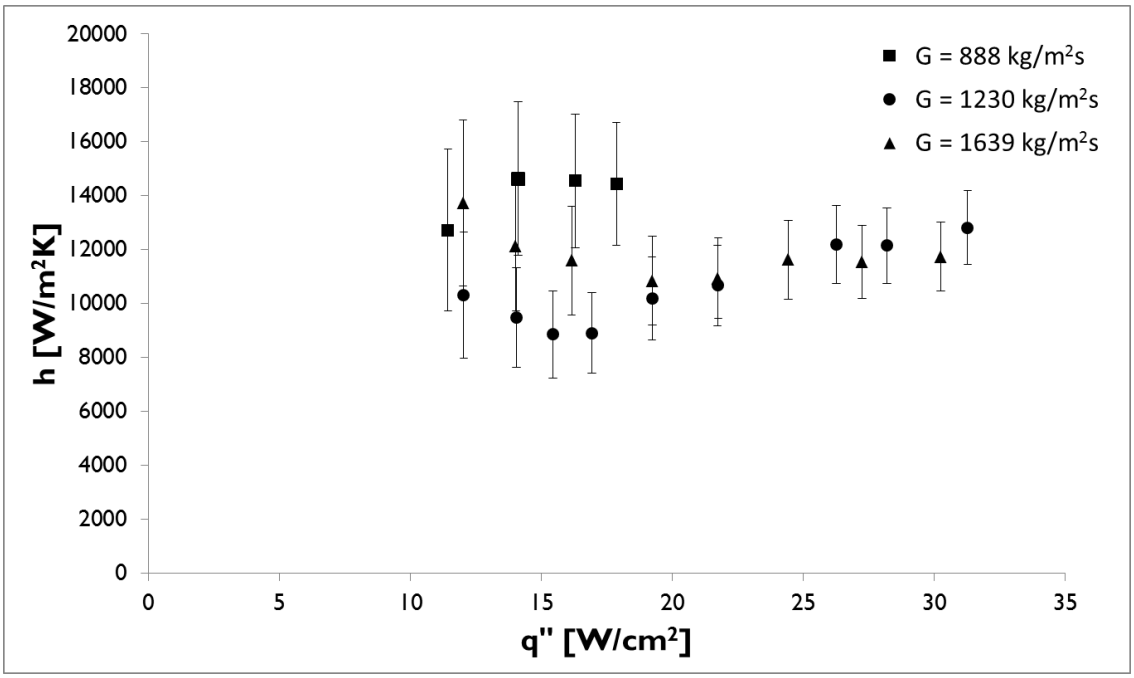

Figure 3.2.5 *h* vs. *q"* for varying flowrate

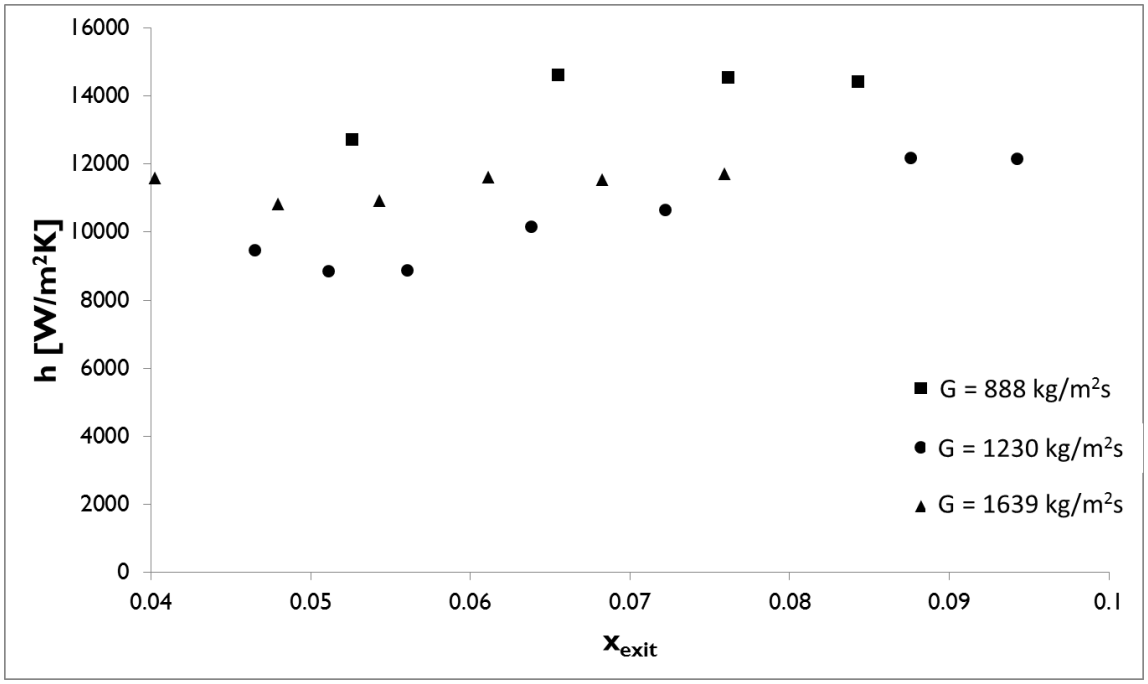

Figure 3.2.6 *h* vs. x_{exit} for varying flowrate

It should be noted that the vapor quality is nearly 50% of that in the uniformly heated case. This was due to the smaller heating area of 1cm x 0.5cm. For a similar heat flux and flowrate range, 1/2 of the heat was required resulting in a substantially lower exit enthalpy. Figures 3.2.7, 3.2.8 and 3.2.9 display flow visualization results for each flowrate. Very little difference is found between flowrates. However, a few interesting observations are noted. For all flowrates considered, bubble departure begins towards the lateral regions of the array and downstream of the active heater. Vapor bubbles form either on the wall of the array, or on pins near the wall and then migrate upstream and towards the center of the array. This is due to the hydrodynamic effect the wall introduces to the flow. For single-phase liquid flow, due to a no-slip condition at the wall, a boundary layer is formed. Without pin fin enhancement the boundary layer thickness would grow from the inlet to the outlet. An increasing boundary layer thickness relates to

an increasing thermal resistance along the wall and, accordingly, an increase in wall temperature.

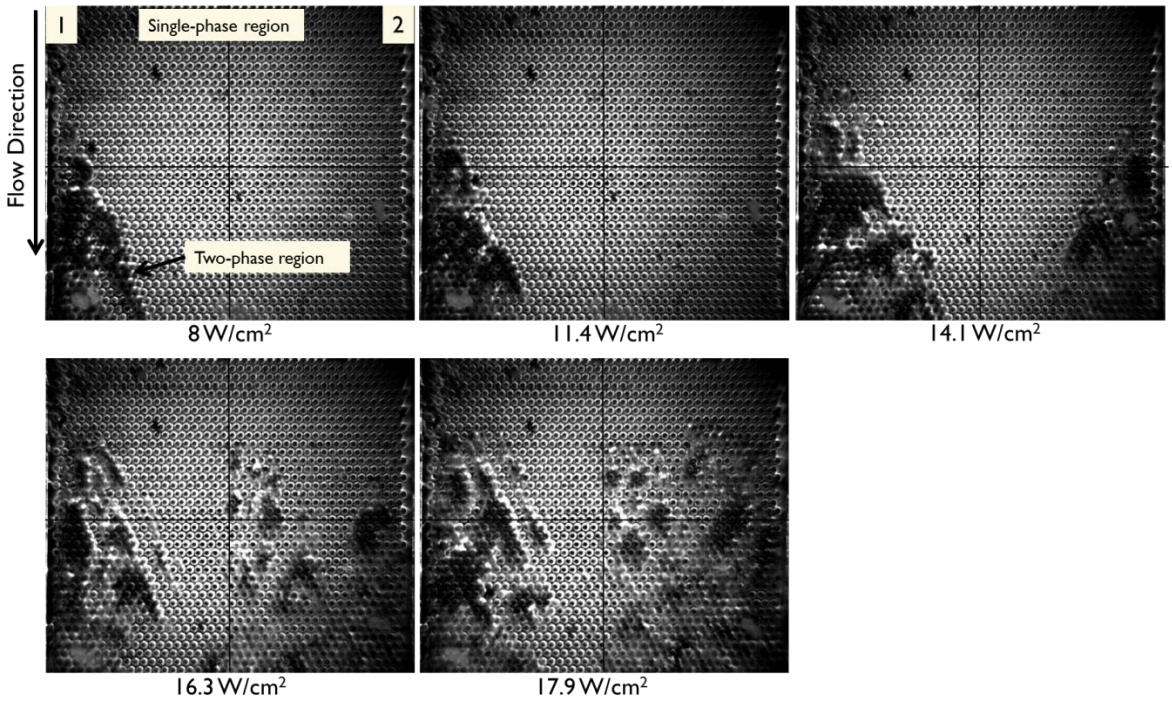

Figure 3.2.7 Flow visualization at G = 888 kg/m^{2}s recorded at a frame rate of 2000 fps

Accordingly, for a pin fin enhanced gap, high surface temperatures may be expected towards the downstream, lateral regions of the array. This reasoning explains the bubble departure point locations at low heat fluxes for this study. This result suggests that, for power map designs, hotspots should be placed in the center of the array. A more in-depth study is required involving local wall temperature measurements to validate this argument. It should be noted that *h* has very little dependence on flowrate, hinting towards possible dry-out conditions. This trend is not consistent with the convective boiling regime in which a change in flowrate leads to a change in vapor velocity. This

results in a change in thickness of the liquid film and, consequently, flowrate dependence for *h*.

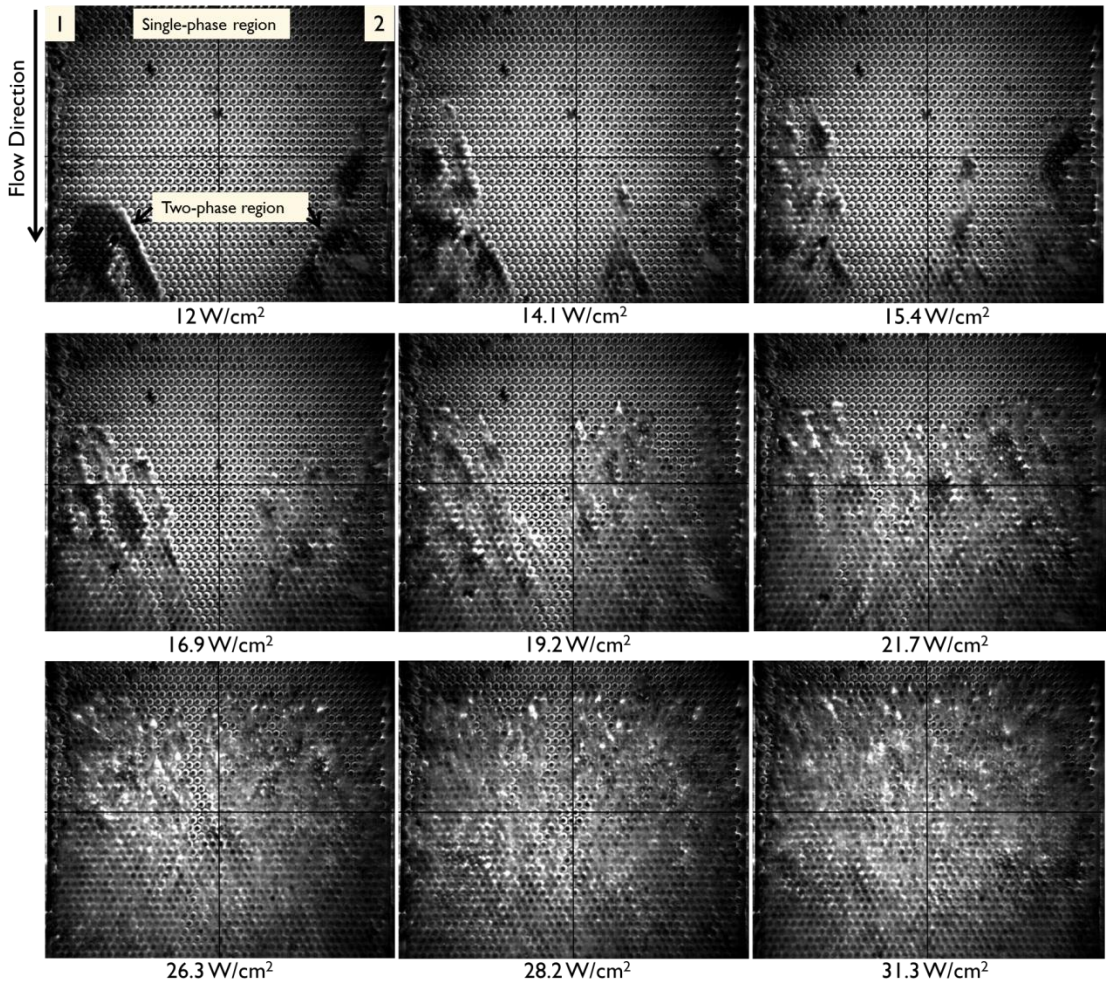

Figure 3.2.8 Flow visualization at G = 1230 kg/m^{2}s recorded at a frame rate of 2000 fps

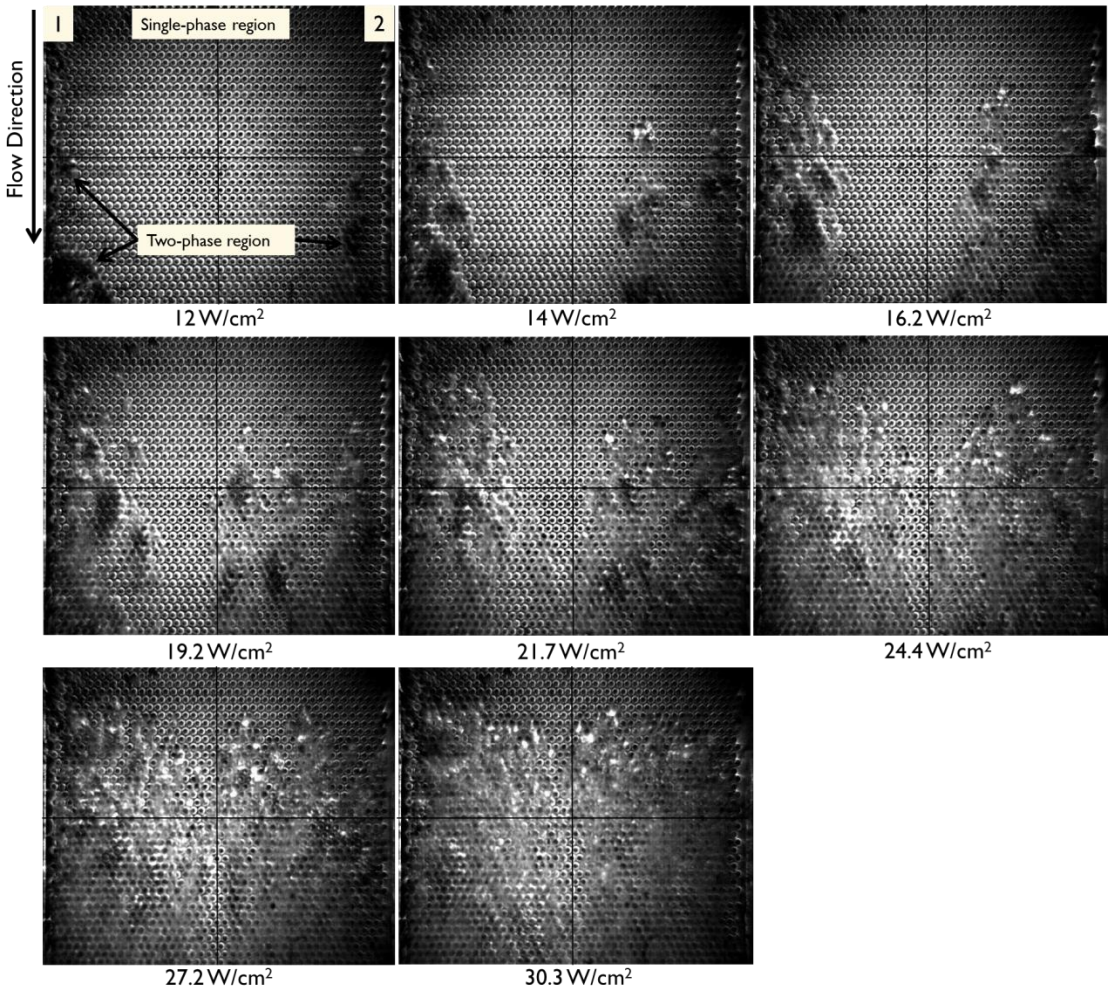

Figure 3.2.9 Flow visualization at G = 1639 kg/m^{2}s recorded at a frame rate of 2000 fps

This partial heating study evaluated the thermal performance of the pin fin array with regards to active, upstream heating. Results for *h* agreed with the uniformly heated sample data and also depicted differences in single to two-phase transition and flow patterns. The rapid transition from single to two-phase conditions suggested an immediate evolution to annular flow with little range for nucleate boiling. A steady plateau of *h* during two-phase conditions centered around 12kW/m^{2}K occurred for a wide range of flowrates. Endwalls located laterally from the array were shown to effect vapor bubble departure patterns. In particular, initial vapor bubble departure locations appeared

near the endwalls. Additionally, vapor wake structure data suggests a strong dependence on surface roughness. Though *h* values are not particullay large, the trends coupled with flow visualization and regime mapping provide an improved understanding of two-phase cooling through a pin fin enhanced micogap.

CHAPTER 4

CONCLUSION

Microscale, liquid cooling devices are at the forefront of possible thermal management methods for modern and future electronic packages. With the advancement of integrated fabrication technologies various geometries such as microchannels and enhanced micro-gaps are capable of being implemented into these high power density packages. Accordingly, the hydraulic and thermal performance of these devices must be evaluated in an effort towards eventual application.

Pin fin enhanced micro-gap devices were fabricated capable of uniform and partial heating. The pins were arranged in a staggered orientation with a height, pitch and diameter of 200μm, 225μm, and 150μm, respectively. A closed flow loop testing platform was constructed capable of running thermal and hydraulic tests of these samples. Heat transfer coefficient values as high as 50 kW/m2K were recorded, in line with relevant experiments in literature. Heat transfer coefficients were strongly dependent on heat flux with minimal dependence on flowrate. Flow regime mapping helped validate the presence of annular flow associated with the convective boiling mechanism. Results of single to two-phase flow conditions indicate a more rapid transition to the convective boiling mechanism with little evidence of the nucleate boiling regime. Flow visualization illustrated conically-shape vapor wakes downstream of bubble departure points revealing a clear advantage over microchannels or other constained geometries. Vapor bubble departure was seen to be strongly dependent on surface roughness features. Partial

heating experiments revealed the effect of the array endwalls on vapor formation suggesting consideration of hotspot placement towards the center of the array.

This study was the first to consider two-phase, diabatic flow through a pin fin enhanced micro-gap. Results demonstrated comparable heat transfer coefficient values under annular flow conditions. This study was also the first to reveal unique vapor wakes within the micro-gap and determine their dependence on applied heat flux and flowrate.

REFERENCES

[1] B. J. Marcinichen, J. Olivier, and J. R. Thome, "Reasons To Use Two-Phase Refrigerant Cooling," in in *Electronics Cooling Magazine*, March., 2011.

[2] D. B. Tuckerman and R. F. W. Pease, "High-performance heat sinking for VLSI," *IEEE Electron Device Letters*, vol. 2, no. 5, pp. 126–129, May 1981.

[3] R. H. . Pijnenburg, R. Dekker, C. C. . Nicole, A. Aubry, and E. H. E. . Eummelen, "Integrated Micro-Channel Cooling in Silicon," in *34th ESSDERC: Solid-State Device Research Conf.*, 2004, pp. 129–132.

[4] W. Qu and I. Mudawar, "Flow boiling heat transfer in two-phase micro-channel heat sinks — I . Experimental investigation and assessment of correlation methods," *International Journal of Heat and Mass Transfer*, vol. 46, pp. 2755–2771, 2003.

[5] W. Qu and I. Mudawar, "Measurement and correlation of critical heat flux in two-phase micro-channel heat sinks," *International Journal of Heat and Mass Transfer*, vol. 47, no. 10–11, pp. 2045–2059, May 2004.

[6] M. B. Bowers and I. Mudawar, "High Flux Boiling In Low Flow Rate, Low Pressure Drop Mini-Channel And Micro-Channel Heat Sinks," *International Journal of Heat and Mass Transfer*, vol. 37, pp. 321–332, 1993.

[7] A. E. Bergles and S. G. Kandlikar, "On the Nature of Critical Heat Flux in Microchannels," *Journal of Heat Transfer*, vol. 127, no. 1, p. 101, 2005.

[8] S. G. Kandlikar, "Fundamental issues related to flow boiling in minichannels and microchannels," *Experimental Thermal and Fluid Science*, vol. 26, no. 2–4, pp. 389–407, Jun. 2002.

[9] J. R. Thome, V. Dupont, and a. M. Jacobi, "Heat transfer model for evaporation in microchannels. Part I: presentation of the model," *International Journal of Heat and Mass Transfer*, vol. 47, no. 14–16, pp. 3375–3385, Jul. 2004.

[10] V. Dupont, J. R. Thome, and a. M. Jacobi, "Heat transfer model for evaporation in microchannels. Part II: comparison with the database," *International Journal of Heat and Mass Transfer*, vol. 47, no. 14–16, pp. 3387–3401, Jul. 2004.

[11] A. Mukherjee and S. G. Kandlikar, "Numerical Simulation Of Growth Of A Vapor Bubble During Flow Boiling Of Water In A Microchannel," in *International Conference on Microchannels and Minichannels*, 2004.

[12] A. Koşar, C.-J. Kuo, and Y. Peles, "Suppression of Boiling Flow Oscillations in Parallel Microchannels by Inlet Restrictors," *Journal of Heat Transfer*, vol. 128, no. 3, p. 251, 2006.

[13] S. G. Kandlikar, "Nucleation characteristics and stability considerations during flow boiling in microchannels," *Experimental Thermal and Fluid Science*, vol. 30, no. 5, pp. 441–447, May 2006.

[14] S. G. Kandlikar, W. K. Kuan, D. a. Willistein, and J. Borrelli, "Stabilization of Flow Boiling in Microchannels Using Pressure Drop Elements and Fabricated Nucleation Sites," *Journal of Heat Transfer*, vol. 128, no. 4, p. 389, 2006.

[15] S. G. Kandlikar, D. A. Willistein, and J. Borrelli, "Experimental Evaluation Of Pressure Drop Elements And Fabricated Nucleation Sites For Stabilizing Flow Boiling In Minichannels And Microchannels," in *3rd International Conference on Microchannels and Minichannels*, 2005, pp. 1–10.

[16] S. G. Kandlikar, "History, Advances, And Challenges In Liquid Flow And Flow Boiling Heat Transfer In Microchannles: A Critical Review," in *14th International Heat Transfer Conference*, 2010, pp. 1–20.

[17] Y. Peles, A. Kosar, C. Mishra, C. Kuo, and B. Schneider, "Forced Convective Heat Transfer Across A Pin Fin Micro Heat Sink," *International Journal of Heat and Mass Transfer*, vol. 48, no. 17, pp. 3615–3627, Aug. 2005.

[18] A. Koşar and Y. Peles, "Thermal-Hydraulic Performance of MEMS-based Pin Fin Heat Sink," *Journal of Heat Transfer*, vol. 128, no. 2, p. 121, 2006.

[19] W. Qu, "Comparison Of Thermal-Hydraulic Performance Of Single-Phase Micro-Pin-Fin And Micro-Channel Heat Sinks," *Components and Packaging Technologies*, vol. 33, no. 1, pp. 105–112, 2010.

[20] T. Brunschwiler, B. Michel, H. Rothuizen, U. Kloter, B. Wunderle, H. Oppermann, and H. Reichl, "Forced Convective Interlayer Cooling in Vertically Integrated Packages," *2008 11th Intersociety Conference on Thermal and Thermomechanical Phenomena in Electronic Systems*, pp. 1114–1125, May 2008.

[21] A. Kosar and Y. Peles, "Micro Scale Pin Fin Heat Sinks — Parametric Performance Evaluation Study," *IEEE Transactions on Components and Packaging Technologies*, pp. 1–11, 2007.

[22] A. Koşar and Y. Peles, "Convective Flow Of Refrigerant (R-123) Across A Bank Of Micro Pin Fins," *International Journal of Heat and Mass Transfer*, vol. 49, no. 17–18, pp. 3142–3155, Aug. 2006.

[23] W. Qu and A. Siu-Ho, “Experimental Study of Saturated Flow Boiling Heat Transfer in an Array of Staggered Micro-Pin-Fins,” *International Journal of Heat and Mass Transfer*, vol. 52, no. 7–8, pp. 1853–1863, Mar. 2009.

[24] S. Krishnamurthy and Y. Peles, “Flow Boiling Heat Transfer on Micro Pin Fins Entrenched in a Microchannel,” *Journal of Heat Transfer*, vol. 132, no. 4, p. 041007, 2010.

[25] Y. Zhang, C. R. K. Jr, J. Zaveri, Y. J. Kim, V. Sahu, Y. Joshi, and M. S. Bakir, “Coupled Electrical and Thermal 3D IC Centric Microfluidic Heat Sink Design and Technology,” pp. 2037–2044, 2011.

[26] J. G. Collier and J. R. Thome, *Convective Boiling and Condensation*, 3rd ed. Oxford, 1994.

[27] Y. Taitel and A. E. Dukler, “A Model for Predicting Flow Regime Transitions in Horizontal and Near Horizontal Gas-Liquid Flow,” *AIChE*, vol. 22, no. 1, pp. 47–55, 1976.

[28] F. P. Incropera, D. P. DeWitt, T. L. Bergman, and A. S. Lavine, *Fundamentals of Heat and Mass Transfer*, vol. 6th. John Wiley & Sons, 2007, p. 997.

[29] B. Agostini, J. R. Thome, M. Fabbri, B. Michel, D. Calmi, and U. Kloter, “High Heat Flux Flow Boiling in Silicon Multi-Microchannels – Part I: Heat Transfer Characteristics of Refrigerant R236fa,” *International Journal of Heat and Mass Transfer*, vol. 51, no. 21–22, pp. 5400–5414, Oct. 2008.

[30] B. Agostini, J. R. Thome, M. Fabbri, B. Michel, D. Calmi, and U. Kloter, “High Heat Flux Flow Boiling in Silicon Multi-Microchannels – Part II: Heat Transfer Characteristics of Refrigerant R245fa,” *International Journal of Heat and Mass Transfer*, vol. 51, no. 21–22, pp. 5415–5425, Oct. 2008.

[31] A. Koşar and Y. Peles, “Boiling Heat Transfer In A Hydrofoil-Based Micro Pin Fin Heat Sink,” *International Journal of Heat and Mass Transfer*, vol. 50, no. 5–6, pp. 1018–1034, Mar. 2007.

[32] S. Krishnamurthy and Y. Peles, “Flow boiling of water in a circular staggered micro-pin fin heat sink,” *International Journal of Heat and Mass Transfer*, vol. 51, no. 5–6, pp. 1349–1364, Mar. 2008.

[33] A. Renfer, M. K. Tiwari, T. Brunschwiler, B. Michel, and D. Poulikakos, “Experimental Investigation into Vortex Structure and Pressure Drop Across Microcavities in 3D Integrated Electronics,” *Experiments in Fluids*, vol. 51, no. 3, pp. 731–741, Apr. 2011.

[34] V. P. Carey, *Liquid-Vapor Phase-Change Phenomena*, 2nd ed. Taylor & Francis, 2008.

[35] S. A. Isaacs, Y. J. Kim, A. J. McNamara, Y. Joshi, Y. Zhang, and M. S. Bakir, "Two-Phase Flow and Heat Transfer in Pin-Fin Enhanced Micro-Gaps," *13th InterSociety Conference on Thermal and Thermomechanical Phenomena in Electronic Systems*, pp. 1084–1089, May 2012.